Journal of Geophysical Research: Solid Earth

RESEARCH ARTICLE
10.1029/2018JB016539

Characteristic Earthquake Magnitude Frequency Distributions on Faults Calculated From Consensus Data in California

Tom Parsons[1], **Eric L. Geist**[1], **Rodolfo Console**[2,3], **and Roberto Carluccio**[2]

[1]United States Geological Survey, Menlo Park, CA, USA, [2]Istituto Nazionale di Geofisica e Vulcanologia, Rome, Italy, [3]Center of Integrated Geomorphology for the Mediterranean Area, Potenza, Italy

Key Points:
- Earthquake magnitude-frequency on faults is suggested to be distributed in an exponential law (Gurenberg-Richter) or characteristic
- We use consensus data from California to solve for the magnitude-frequency distribution on all known faults in the state
- We find that individual faults have characteristic magnitude distributions

Correspondence to:
T. Parsons,
tparsons@usgs.gov

Citation:
Parsons, T., Geist, E. L., Console, R., & Carluccio, R. (2018). Characteristic earthquake magnitude frequency distributions on faults calculated from consensus data in California. *Journal of Geophysical Research: Solid Earth*, *123*, 10,761–10,784. https://doi.org/10.1029/2018JB016539

Received 10 AUG 2018
Accepted 21 NOV 2018
Accepted article online 28 NOV 2018
Published online 15 DEC 2018

Abstract An estimate of the expected earthquake rate at all possible magnitudes is needed for seismic hazard forecasts. Regional earthquake magnitude frequency distributions obey a negative exponential law (Gutenberg-Richter), but it is unclear if individual faults do. We add three new methods to calculate long-term California earthquake rupture rates to the existing Uniform California Earthquake Rupture Forecast version 3 efforts to assess method and parameter dependence on magnitude frequency results for individual faults. All solutions show strongly characteristic magnitude-frequency distributions on the San Andreas and other faults, with higher rates of large earthquakes than would be expected from a Gutenberg-Richter distribution. This is a necessary outcome that results from fitting high fault slip rates under the overall statewide earthquake rate budget. We find that input data choices can affect the nucleation magnitude-frequency distribution shape for the San Andreas Fault; solutions are closer to a Gutenberg-Richter distribution if the maximum magnitude allowed for earthquakes that occur away from mapped faults (background events) is raised above the consensus threshold of $M = 7.6$, if the moment rate for background events is reduced, or if the overall maximum magnitude is reduced from $M = 8.5$. We also find that participation magnitude-frequency distribution shapes can be strongly affected by slip rate discontinuities along faults that may be artifacts related to segment boundaries.

Plain Language Summary While we know that in large regions, earthquakes obey an exponential distribution (Gutenberg-Richter), it has been unclear whether individual faults do as well, or whether they follow a characteristic distribution. We find using three new methods to solve for the earthquake rate on California faults that all solutions are consistent with characteristic distributions, with greater numbers of large earthquakes relative to small than expected from a Gutenberg-Richter trend.

1. Introduction

The magnitude frequency distribution on individual faults matters because the specific rate of earthquakes of a given size at each source point has important influence on probabilistic seismic hazard assessment (Cornell, 1968), and thus on building codes and public safety. For example, the amplitude and period of strong shaking is distance and magnitude dependent; a balance tilted toward frequent moderate magnitude versus infrequent very large earthquakes emanating from a particular source point has different implications over a fixed design period on a hazard map.

It is demonstrated that the earthquake magnitude frequency distribution follows a negative exponential trend in large regions that contain multiple faults (Gutenberg & Richter, 1954; Ishimoto & Iida, 1939), which is usually referred to as the Gutenberg-Richter distribution. Studies of individual faults through paleoseismology and earthquake catalog data sometimes support alternative distribution shapes that are called characteristic, where there is more than one mode within the size distribution on a given fault (e.g., Hecker et al., 2013; Ishibe & Shimazaki, 2012; Papadopoulos et al., 2003; Schwartz & Coppersmith, 1984; Sykes & Ekström, 2012; Wesnousky, 1994). Alternatively, arguments are made for Gutenberg-Richter distributions applying to individual faults and/or that the data are insufficient to resolve the question (e.g., Page et al., 2011; Page & Felzer, 2015; Parsons et al., 2012; Parsons & Geist, 2009; Stein & Newman, 2004). Still others opine that the issue is dead (Kagan et al., 2012) and that there can be no debate (Geller et al., 2015; Mulargia et al., 2017), although there was literally a debate as recently as the 2010 Seismological Society of America Annual Meeting (Page, 2010; Schwartz, 2010). Whether there is a debate or not, there are examples of characteristic earthquake rate distributions, Gutenberg-Richter distributions, or a combination of both being applied for hazard calculations

(e.g., Cornell, 1968; Field et al., 2009, 2014; Mazzotti et al., 2011; Mezcua et al., 2011; Petersen et al., 2014; Stirling & Gerstenberger, 2018).

We note that there are different interpretations of what a characteristic earthquake distribution means that can be combined with arguments for or against periodic earthquake interevent times and/or seismic gaps (e.g., Geller et al., 2015; Mulargia et al., 2017; Rong et al., 2003). Here we are concerned with the shape of the long-term earthquake size distribution on individual faults, and we define a characteristic distribution as having more than one mode such that there is significant deviation from an exponential trend. We do not comment on issues around periodicity or seismic gaps, which are not relevant to time independent hazard assessments.

There are difficulties associated with directly observing the magnitude frequency distribution on active faults because location uncertainty associated with lower magnitude and/or nonsurface rupturing shocks means that we can never be sure if such earthquakes occur directly on a major fault surface or on a nearby subsidiary fault, a problem that gets increasingly worse in older catalogs. Additionally, the largest earthquakes occur infrequently relative to observation periods, meaning there is uncertainty whether we have a complete record for individual faults, or have witnessed their maximum magnitudes (e.g., Geist & Parsons, 2014). There are two ways one can view the magnitude rate on faults. Nucleation magnitude-frequency means that each earthquake in the distribution has its hypocenter located on the fault surface area in question, and thus began there. Participation magnitude-frequency means that earthquake ruptures that began on any other fault area and then spread onto the fault surface in question are counted in the distribution. The shape of the nucleation magnitude-frequency is most interesting in understanding earthquake mechanics, whereas the participation magnitude-frequency distribution is most applicable in calculating hazard at a given point because all nearby sources of shaking must be accounted for.

Page et al. (2014) developed a simulated annealing solution to invert for the rates of all possible ruptures (after Andrews & Schwerer, 2000; Field & Page, 2011; Field et al., 2014) above a threshold magnitude on a fault array by using the constraints of observed regional earthquake rates, *b* values, and fault slip rates, along with other observations. Application of this method for the Uniform California Earthquake Rupture Forecast 3 (UCERF3) used a characteristic nucleation magnitude frequency constraint on major fault lines like the San Andreas (Field et al., 2014; Page et al., 2014), in part to match results from the prior forecast (UCERF2; Field et al., 2009), and because efforts to enforce Gutenberg-Richter distributions to faults were not successful (Field et al., 2014). Magnitude frequency results for individual fault sections make very specific characteristic predictions; for example, on the North Mojave section of the San Andreas Fault, the expected nucleation rate of M~8.0 earthquakes is 25 times higher than for M~6.6 earthquakes, and the participation rate distribution has a similar shape (Field et al., 2014; Figure 1). Therefore, it is not only important to establish whether faults depart from Gutenberg-Richter distributions, but also by how much at every magnitude level.

We revisit the earthquake rupture rate distribution question on California faults by bringing three additional methods to bear on the problem. We hope to minimize possible methodological influences by applying more methods, and to learn more about what features in the data most affect magnitude-frequency distributions. We work in California because the UCERF3 effort amassed, unified, and vetted published data, uncertainties, and models through a community consensus process to acquire the legally mandated "best available science" (Field et al., 2014). We thus eliminate potential bias related to decisions about which data to include/exclude that might influence the results. These data include a collection of defined California faults (Figure 2) that were confirmed as active through published geologic maps and fault-by-fault open forum expert opinion (Dawson, 2013). Fault slip rates were assembled from published geologic offset observations and a series of geodetic models (Parsons et al., 2013). Consensus fault linkages and rupture filtering (Biasi et al., 2013; Milner et al., 2013), as well as earthquake catalogs/projected annual rates, and *b* values (Felzer, 2013a, 2013b) were developed. Additionally, a compilation of paleoseismic recurrence data was assembled by Weldon, Schmidt, et al. (2013), as well as observed fault creep rates (Weldon, Dawson, et al., 2013).

We focus primarily on the San Andreas Fault because it is the longest in California, and can thus host a magnitude range from the smallest events considered up to a theoretical complete rupture of its full length, which would be a M~8.5 shock depending on the magnitude-area relation used to calculate it. The San Andreas Fault also has the highest slip rates in California, causing it to produce the largest number of earthquakes; this provides larger samples for establishing the magnitude frequency relations in solutions

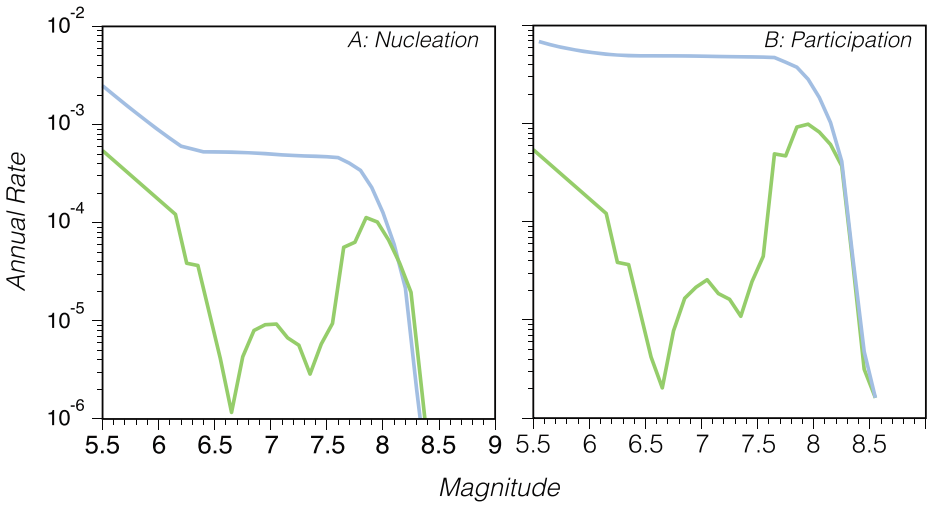

Figure 1. Magnitude frequency distribution for (a) earthquake nucleation and (b) earthquake participation on the north Mojave section of the San Andreas Fault after Field et al. (2014). Cumulative distributions are shown in blue and incremental in green. Both the participation and nucleation distributions appear characteristic, with more *M*~8 events than *M*~7.

calculated over fixed time scales. Over hundreds of kilometers of the fault length, a rich variety of multisegment ruptures and earthquake branching behaviors onto subsidiary faults can be included without concern about arbitrary fault end points affecting the solutions. Calculations presented here solve for earthquake rate distributions on every California fault, so we do explore additional fault zones.

2. Methods

The 2014 UCERF3 time-independent earthquake rate model (Field et al., 2014) serves as the benchmark study for California faults. Because this model was a consensus process with acknowledged subjective components, we compare its results to those from three independent methods that use the same data inputs. Each of

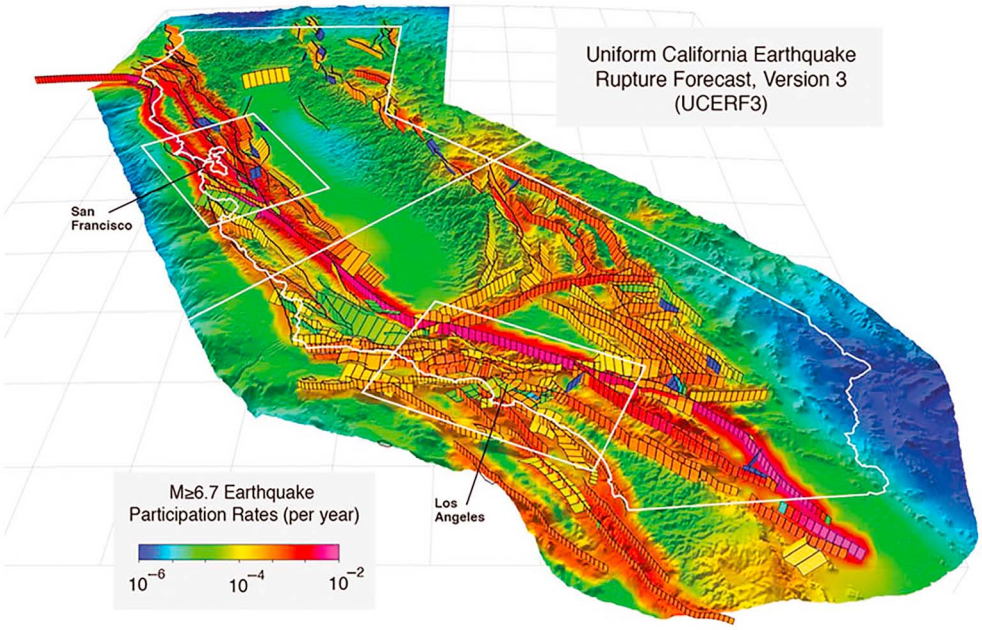

Figure 2. The UCERF3 fault model is shown shaded by long-term participation rates for $M \geq 6.7$ earthquakes (Field et al., 2014). The model represents expert consensus on known active faults in California, and was vetted through open meetings. Earthquakes occur away from known faults, and are referred to as "background seismicity." Thus, color shading away from mapped faults represents the long-term $M \geq 6.7$ rate from background events.

these methods has been published, and full details about them can be found in the given citations, but we supply basic descriptions of them here.

All of these methods solve for the earthquake rate on mapped faults, constrained primarily by observed/modeled slip rates. It is clear however that earthquakes occur in California at locations not associated with any mapped faults. Thus, some proportion of seismicity is referred to as "background earthquakes." The total annual moment rate from the observed earthquake catalog is $2.29 \cdot 10^{19}$ Nm/year, and the mean of UCERF3 solutions resulted in $1.86 \cdot 10^{19}$ Nm/year of that occurring on mapped faults, with another $0.29 \cdot 10^{19}$ Nm/year as background earthquakes (Field et al., 2014); this balance is a direct consequence of the moment implied by the consensus fault slip rate model. Our new methods target this balance of on-fault and background moment, and all three rely on input earthquake lists constrained by statewide *a* and *b* values (Felzer, 2013b) for fixed times (4–100 kyr depending on the method) constrained to be Gutenberg-Richter over the entire study region. No spatial variation in *a* values is used; thus, the results have no dependence on observed off-fault seismicity rates. We are able to calculate smaller on-fault earthquake rates than the UCERF3 methods because of smaller discretization of the fault model (2 km by 2 km in some cases). Off-fault moment is not solved for, but instead, background events are removed by magnitude-frequency according to the Gutenberg-Richter distribution from the input catalogs up to the maximum off-fault magnitude, which ranges between $M = 7.3$ and $M = 7.9$, with heaviest weight (0.8) at $M = 7.6$ (Field et al., 2014). The consensus models we run use the $M = 7.6$ value, but we explore the effects of alternate maximum background earthquake magnitudes.

2.1. UCERF3 Grand Inversion

The UCERF3 model framework defined the long-term rate of all possible earthquake ruptures above a magnitude threshold ($M \geq 5$) on defined faults and accounted for earthquakes that might happen in areas where no faults are known. Defined faults were divided into subsections sized by a width that extended from the top to the bottom of the seismogenic area, and a length that was half the seismogenic width. Ruptures were represented by a minimum of two subsections (M~6) and could grow into large collections of adjacent or nearby subsections. Earthquakes with magnitudes smaller than M~6 are termed "subseismogenic on-fault ruptures," and their rates were quantified from gridded smoothed background seismicity rates that were mapped within polygons (~5–10 km wide) drawn around fault zones. Each earthquake rupture is assigned a hypocenter location at random, with a uniform probability of nucleating anywhere along its length.

Key features of the UCERF3 rate model included allowing ruptures to jump from fault to fault, and not restricting ruptures to occur within predefined fault sections. Both of these changes from the UCERF2 approach (Field et al., 2009) greatly increased the set of possible earthquake ruptures, which in turn increased the computational demands in finding rate solutions. Rupture filtering was introduced to eliminate nonsensical ruptures, and to make the problem more tractable (Milner et al., 2013) as

1. All fault sections connect within 5 km or less, as assessed by Biasi et al. (2013).
2. Ruptures cannot include a subsection more than once.
3. Ruptures must contain at least two subsections of any main fault section, unless the only way two fault sections can connect is through a single-subsection connector, as described by Milner et al. (2013).
4. Ruptures can only jump between fault sections at their closest points (in 3D).
5. The maximum azimuth change between the first and last subsection within a rupture is 60°, except for left-lateral to right-lateral connections such as Garlock to the San Andreas. This is done to eliminate U-turn and circular ruptures.
6. The maximum cumulative rake change (summing over each neighboring subsection pair) is 180°, based on observed rakes to ensure rupture-set consistency.
7. The maximum cumulative azimuth change, computed by summing absolute values over each neighboring subsection pair, is less than 560° (a filter that reduces "squirreliness," that is, many changes of azimuth).
8. Branch points (potential connections between main fault sections) must pass a Coulomb criterion that earthquake triggering between the two fault sections is physically reasonable, as described by Milner et al. (2013).

The inversion method estimated the long-term rates of viable ruptures by solving a system of equations that represent data constraints on possible earthquake rates including observed slip rates, paleoseismic

earthquake rates, the observed regional seismicity rates from historic earthquake catalogs, smoothness constraints, and other optional solution features (Field et al., 2014). The equations were weighted by data uncertainties and expert opinion. In addition to setting equation set weights, there were also subjective weights added to alternative logic tree branches guided by how well models fitted the data. A parallelized code was developed to efficiently solve very large equation sets by simulated annealing (Page et al., 2013), and high-performance compute resources were required to obtain thousands of solutions in a reasonable amount of time. Simulated annealing provided a range of models that sampled the under determined solution space of the inverse problem to represent the epistemic uncertainty associated with model nonuniqueness.

One key difference between the UCERF3 Grand Inversion and the three alternative methods presented here is the use of target magnitude-frequency distributions, which can be either Gutenberg-Richter or characteristic. Viable Gutenberg-Richter solutions were not found in the UCERF3 application (Field et al., 2014), so characteristic target magnitude-frequency distributions on faults were defined to have one third of the slip rate dedicated to a Gutenberg-Richter distribution that is a combination of nearby gridded seismicity (subseismogenic) and on-fault earthquakes, and the other two thirds is expressed as maximum magnitude events. The new methods that we apply here do not have target magnitude-frequency distributions because we want to independently assess the magnitude-frequency shape. We also do not use observed gridded seismicity rates because the faults can be discretized into smaller areas, so that lower magnitude events can be solved for directly.

2.2. Optimization With Integer Programming

Distributing earthquakes among a system of faults with finite slip can be described as a combinatorial optimization problem (Korte & Vygen, 2014) where possible solutions are found through complete enumeration from all possible combinations (Chen et al., 2010). Two common approaches to solve combinatorial optimization problems include integer programming and greedy algorithms, the latter used by the greedy sequential method described in section 2.4. Integer programming is the first independent method we apply and is similar to linear programming, which are both composed of a linear objective function that is minimized or maximized subject to a series of constraints (Chen et al., 2010; Williams, 2013; Wolsey, 1998). Integer programming, as applied to the earthquake rate problem, involves binary variables (decision vector) representing all possible locations of earthquakes in the fault system, optimized to minimize the slip rate misfit among all faults. Earthquakes used in the optimization are sampled from a state wide Gutenberg-Richter distribution (Figure 3a) over a 4-kyr period using the consensus a and b values from the UCERF3 model and taking into account background seismicity. Ruptures are assumed to be rectangular with area determined from magnitude using the Wells and Coppersmith (1994) scaling relation. Mean event slip is found using the moment-magnitude relation (Hanks & Kanamori, 1979) assuming a shear modulus of $\mu = 30$ GPa. Ruptures are allowed to overlap, and each earthquake in the 4-kyr sample must be used once and only once. This method does not identify earthquake nucleation sites because whole rupture slip areas are fit onto the faults simultaneously. Nucleation sites could be assigned at random in similar fashion as the UCERF3 inversion.

The approach described by Geist and Parsons (2018) uses general mixed integer programming solvers. These solvers apply a variety of methods to limit the solution space, and make very large problems such as this (~2.5 million variables) possible. First, the integer constraint is relaxed and an initial solution is obtained as if it was a linear programming problem using the simplex algorithm. This forms the root of a search tree that conceptually contains all integer solutions. The next level of the search tree is defined by the closest integer solutions to the relaxed solution. Of these, the solutions that satisfy all the constraints are termed feasible solutions, and branching proceeds with the solution that has lowest objective function, since this is a minimization problem. At each step, there are a number of algorithms that can provide bounds to possible solutions that makes the search process much more efficient (Chen et al., 2010). In addition, branching techniques have been developed to identify infeasible paths or paths that result in inferior solutions, thus limiting the search space (Klotz & Newman, 2013; Morrison et al., 2016). Outputs can include either optimal or feasible solutions; the latter satisfy the constraints but no objective function is given. Similarly to the UCERF3 solutions, the minimum magnitude solved for is M~6 to make integer-programming solutions tractable on high-performance compute platforms.

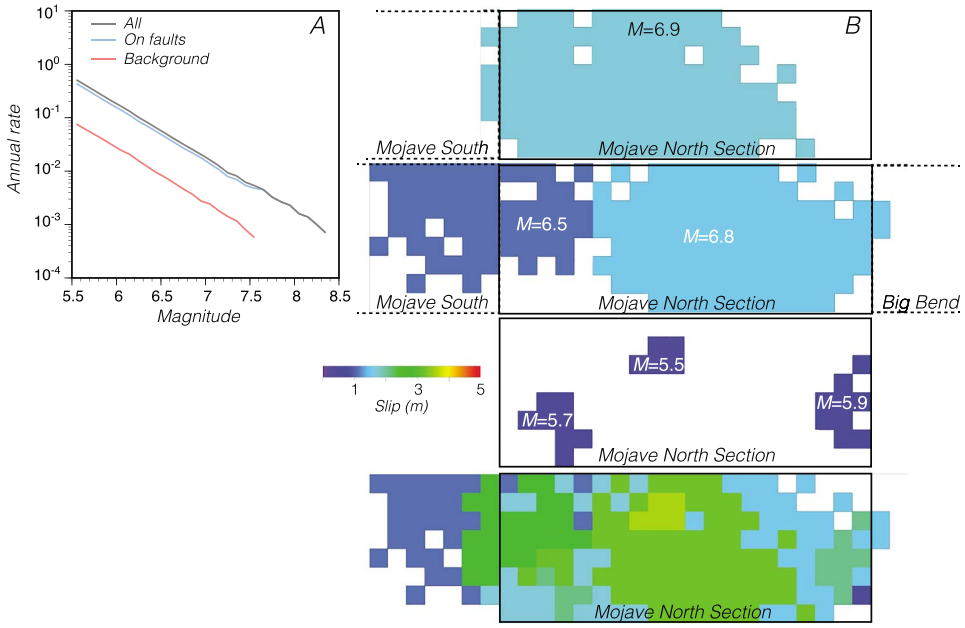

Figure 3. Example ruptures from the north Mojave section of the San Andreas Fault. Earthquakes have uniform slip scaled to magnitude, but can take any contiguous shape. Individual ruptures are shown in the top 3 panels, and are combined in the bottom one. (a) Ruptures are drawn sequentially from the "on-fault" input magnitude-frequency curve in the greedy sequential, as well as the integer programming and the stress simulator methods, and (b) evolve in the greedy sequential method to fill slip gaps until the 100-kyr slip budget is satisfied on all California faults. Cells are 2 km by 2 km.

2.3. Stress-Based Earthquake Simulator

The second independent method we apply is a physics-based earthquake simulator (Console et al., 2015, 2017) where the seismogenic system is modeled by rectangular fault sections. Each section is composed of many square cells of size set to the minimum earthquake rupture of interest (M = 5.0 in this case). Each cell has an initial stress state that is randomly assigned. Then each cell is loaded at a steady state proportional to UCERF3 slip rates (weighted average of four slip rate models for California faults based on geologic offsets and geodetic data (Parsons et al., 2013)) to simulate tectonic stressing. A cell can nucleate an earthquake if its stress value crosses an assigned strength threshold. The method thus provides a physical basis for earthquake nucleation points. After nucleation occurs, the stress state of all other cells in the model is changed through static stress transfer. Dynamic rupture propagation is simulated by a reduction of the effective strength in neighboring cells within a specified search area. The strength reduction is limited if the search area exceeds a given aspect ratio of the rupturing section, which discourages rupture propagation. A rupture stops when there are no cells with effective strength above the threshold value within the search area. A cell can rupture more than once in the same event. The method is similar to other earthquake simulators (e.g., Tullis, 2012); in that, it is stress-driven. However the method relies primarily on static Coulomb stress evolution, and is thus simpler with relatively few parameters because it does not apply rate/state friction, viscoelasticity, or fully dynamic ruptures.

The final estimate of the seismic moment of an earthquake is obtained from the sum of the moment released by each ruptured cell. The mean event slip is then computed from the total seismic moment and the total ruptured area. Magnitude is found using the moment-magnitude relation (Hanks & Kanamori, 1979) assuming a shear modulus of μ = 30 GPa.

A rupture can propagate between two defined sections if the distance between them is less than a given value (5 km in this application). The simulation algorithm preferentially fills rupture gaps by nucleating events in cells where the stress budget is higher. Ruptures also expand toward parts of the faults where the stress budget is highest. Because of the stress transfer included in the model, ruptures tend to initiate close to the termination points of preceding large earthquakes. Calculations were run to simulate 100-kyr durations to minimize time-dependent effects on earthquake rates.

Key inputs that govern dynamic rupture propagation and that affect solutions are a strength reduction coefficient (SR) and an aspect ratio coefficient (AR). After a simulated earthquake nucleates, the effective strength of the cells in the area surrounding is reduced by a value proportional to the square root of the search area, which allows the rupture to expand. This affects the maximum magnitude of ruptures. This strength reduction is limited if the search area exceeds a given number of times the width of the rupturing section, through the AR coefficient. This acts to discourage rupture expansion.

2.4. Greedy Sequential Algorithm

The third independent method we apply is termed the greedy sequential algorithm. Greedy algorithms solve combinatorial problems by selecting the highest value objects first under the assumption that an answer that approximates the optimal solution will result (e.g., Cormen et al., 2009; Korte & Vygen, 2014). Their advantage is that they do not operate on the entire solution space simultaneously, but instead work sequentially, making it possible to address the California earthquake rate solution without memory demands of high-performance computer resources. The key assumption is that an approximately optimal solution results from the most difficult-to-fit highest-magnitude earthquakes being solved for first. Lower magnitude events are more easily fit into small gaps in the slip budget left after the larger events are placed. In our application (Parsons et al., 2012; Parsons & Geist, 2009), the algorithm attempts to fit earthquakes into the connected fault system, working from the highest magnitudes to the lowest in sequence as selected from a Gutenberg-Richter distribution using the consensus *a* and *b* values from the UCERF3 model (Felzer, 2013b). Following UCERF3, the preferred data parameter set has 16% of the total seismic moment release being assigned to background earthquakes that occur away from known mapped faults, with the maximum magnitude of those events being M = 7.6 (Field et al., 2014; sensitivity of results is tested by varying these parameters).

We begin to populate the simulation with earthquake ruptures by randomly assigning earthquake nucleation sites distributed in proportion to slip rates, such that the highest slip rate parts of the fault are most likely to nucleate the largest events. Trial hypocenter locations are attempted until each earthquake is fit within a set of 2 × 2-km cells; small cell sizes mean that irregularly shaped ruptures can occur that may be more realistic, and that do not require a surface rupture (Figure 3). Nucleation points therefore have an initially random component, but are subsequently positioned where less slip has occurred during the model run, which is a proxy for increased stress. Rupture areas are determined from the "Ellsworth B" empirical magnitude-area relation $M_w = \log(A) + 4.2$ [WGCEP (Working Group on California Earthquake Probabilities), 2003]. Fitting is constrained by the long-term slip rates of faults, and a 100-kyr slip budget is assigned to each cell based on the weighted average of four slip rate models for California faults from geologic offsets and geodetic data (Parsons et al., 2013). The same set of rules for fault jumping and rupture filtering are followed as listed in section 2.1. We calculate mean event slip from the moment-magnitude relation (Hanks & Kanamori, 1979) assuming a shear modulus of μ = 30 GPa.

Calculations for all of California usually take approximately four days to complete on a standard laptop computer, depending on the number of earthquakes in the input catalog; one calculation that used the maximum California *a* value took ~40 days to run. The algorithm can be inefficient because random hypocenter locations are repeatedly attempted until each earthquake can be fit into the fault system within the 100-kyr slip budget. More guided simulations like the stress-based simulator described previously are more efficient.

2.5. Measuring Differences Between Magnitude-Frequency Distributions

The primary question we address is, how great is the relative deviation of an individual fault magnitude frequency distribution from Gutenberg-Richter? We use test statistics and *p* values from three nonparametric statistical methods to assess the degree that calculated magnitude-frequency distributions vary from Gutenberg-Richter. These test include the Kolmogorov–Smirnov test (Kolmogorov, 1933; Smirnov, 1933), which is a standard approach to testing exponential distributions (e.g., Clauset et al., 2009), the Wilcoxon rank-sum test (also known as the Mann–Whitney test; Mann & Whitney, 1947; Wilcoxon, 1945), and the Epps-Singleton test (Epps & Singleton, 1986). We compare calculated earthquake catalogs to a catalog generated by drawing 5,000 earthquakes at random from a theoretical Gutenberg-Richter distribution (b = 1; Felzer, 2013b) across the possible magnitude distribution to assess whether they can have the same origin.

The two-sample Kolmogorov–Smirnov test compares an empirical distribution function $F(x)$ against a second sample from a theoretical cumulative distribution $G(x)$ for equality. It tests hypotheses that the empirical group has smaller or larger values than the theoretical as

$$D^+ = \max\{F(x) - G(x)\}$$

$$D^- = \min\{G(x) - F(x)\}$$

and then finds the maximum difference, which yields the test statistic D by

$$D = \max\{|D^+|, |D^-|\}$$

We use the Stata© program to find the first five terms (P_a) of the asymptotic limiting distribution

$$\lim_{m,n\to\infty} \Pr\left\{\sqrt{mn/(m+n)}D_{m,n} \le z\right\} = 1 - 2\Sigma_{i=1}^{\infty}(-1)^{i-1}\exp\left(-2i^2z^2\right),$$

which are used to calculate corrected p values with a numerical technique (Z) where Φ is the cumulative normal distribution as

$$Z = \Phi^{-1}(P_a) + 1.04/\min(m,n) + 2.09/\max(m,n) - 1.35/\sqrt{mn/(m+n)}$$

and p value thresholds can be found from the cumulative normal distribution of the numerical values as p value = $\Phi(Z)$.

The second methods we use is the Wilcoxon rank-sum test, which compares two independent random variables F and G with sample sizes n and m with the null hypothesis that $F = G$. The samples are combined and ranked (R_i), and the Wilcoxon test statistic T is found from the sum of the ranks of a sample as

$$T_F = \Sigma_{i=1}^{n} R_{Fi}$$

The Mann–Whitney U statistic is the number of pairs (F_i,G_j) such that $F_i > G_j$, or $G_i < F_j$, and is given by

$$U = \min(U_F, U_G)$$

where

$$U_F = nm + \frac{n(n+1)}{2} - T_F$$

$$U_G = nm + \frac{m(m+1)}{2} - T_G$$

The variance and standard deviation (σ) of the combined ranks are found by

$$Var(T) = \frac{nm\sigma^2}{n+m}, \sigma^2 = \frac{1}{n+m-1}\Sigma_{i=1}^{n+m}\left(R_i - \overline{R}\right)^2$$

For large samples, the distribution of ranks can be treated as normal (although the test is valid for all distribution forms), and a z statistic (number of standard deviations from the mean) can be used to calculate p values as

$$z = \frac{T - \frac{n(n+m+1)}{2}}{\sqrt{Var(T)}}$$

where if Z is a normal distribution from 0 to 1, then

$$p = \Pr(Z \ge z).$$

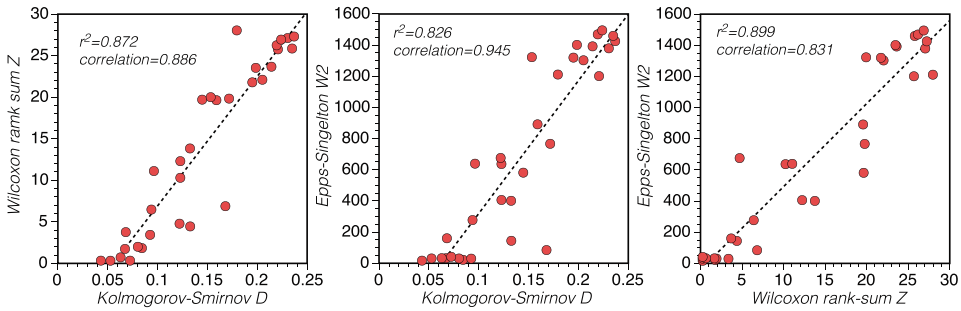

Figure 4. Correlations between three test statistics made from comparisons of San Andreas Fault earthquake nucleation magnitudes to a Gutenberg-richer distribution. Correlations are strong, ranging from 0.83 to 0.95, and the linear models explain between 83 and 90% (r^2 values) of the scatter. We interpret these correlations as independent statistical methods identifying the same differences between calculated magnitude-frequency distributions and the null model, a Gutenberg-Richter distribution.

The third method we use is the Epps-Singleton test as implemented for Stata© by Goerg and Kaiser (2009). This method is important because it does not require the test samples to be from continuous distributions. All of the methods we used to calculate the magnitude distribution in California faults use discretized fault representations. This means the resulting magnitudes, which can be carried out to many decimal places, are still not completely continuous because they are a direct function of areas, of which there are a finite number. The Epps-Singleton test is similar to the Kolmogorov–Smirnov test except that it uses empirical characteristic distribution functions, which are the Fourier transforms of the empirical distribution functions. This difference allows discrete data to be compared.

The null hypothesis is that the empirical characteristic distribution functions of distributions *F* and *G* are equal as

$$\phi(t) = \gamma(t), \text{with} -\infty < t < \infty.$$

The empirical characteristic distribution function of $F_{nk}(x)$ is defined as

$$\phi_{nk} = \int_{\infty}^{-\infty} e^{itx} dF_{nk}(x) - n_k^{-1} \Sigma_{m=1}^{nk} e^{itX_{km}}.$$

The test statistic W_2 measures the statistical distance between the empirical characteristic distribution functions of both samples standardized by the covariance matrix ($\widehat{\Omega}$) as

$$W_2 = (n+m) \cdot \Delta' \cdot \widehat{\Omega}^{+} \cdot \Delta,$$

where Δ is the difference between the real and imaginary parts of the characteristic function of the samples and $\widehat{\Omega}^{+}$ is the generalized inverse of $\widehat{\Omega}$. The test statistic is distributed asymptotically as chi-square with *r* degrees of freedom, where *r* is the rank of $\widehat{\Omega}^{+}$, which is how the *p* value of the test is found.

For each statistical test, we compare earthquake nucleation and participation catalogs ($M \geq 6.0$) from the three calculation methods we use as well as from UCERF3 against the same 5,000-point sample catalog drawn from a Gutenberg-Richter distribution with a *b* value equal to 1. The null hypothesis is therefore that the calculated catalogs cannot be distinguished from Gutenberg-Richter. The standard for rejection of a null hypothesis is a *p* value less than 0.05, although caution is urged about absolute thresholds (e.g., Wasserstein & Lazar, 2016). We therefore conclude that the Gutenberg-Richter null hypothesis cannot be rejected if all three statistical tests return *p* values >0.05.

We note consistency among the three statistical methods applied because the independent test statistics can be correlated. An example is shown in Figure 4 of test statistics made comparing multiple nucleation magnitude-frequency distributions from four methods calculated using an array of different input parameters. We find strong correlations (coefficients range from 0.83 to 0.95) between the test statistics, and

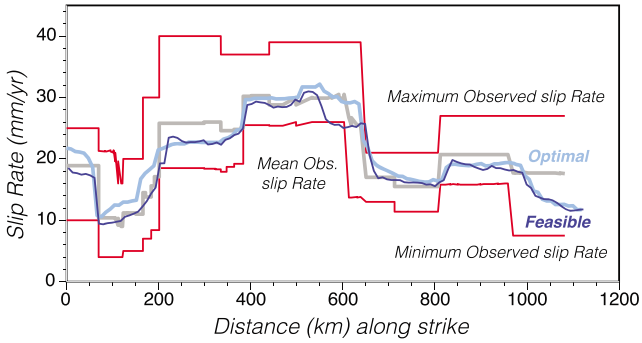

Figure 5. Slip rate fits from integer programming are shown along strike of the San Andreas Fault. The red lines bracket the minimum and maximum UCERF3 slip rates, the gray line is the weighted mean UCERF3 slip rate, the blue line is the model calculated slip rate from the average of ten optimal solutions, and the yellow line is the average of ten feasible solutions.

simple linear models explain between 83 and 90% of the scatter in the correlations. We interpret these correlations as an indication that the three tests we apply are identifying the same variations between calculated magnitude-frequency distributions and the null model of a Gutenberg-Richter distribution. We further can apply the test statistics as a means to rank the different calculation results in terms of their relative difference/similarity to a Gutenberg-Richter distribution to understand the effects of data and calculation parameters. Any of the test statistics would be reasonable to use for ranking given how closely correlated they are; we choose the Epps-Singleton W_2 statistic for ranking because that test is not vulnerable to discrete data. We express the degree that a solution differs from Gutenberg-Richter by calculating the ratio of the W_2 statistic to the constant critical value (9.488) that yields a p value of 0.05. When this parameter that we label as the *ES factor* is $\leq$1.0, then a Gutenberg-Richter distribution cannot be ruled out at 95% confidence. The degree to which values grow much larger than 1.0 indicates the strength of deviation from a Gutenberg-Richter distribution.

3. Results

We compare results from four techniques for solving the earthquake rate and magnitude distributions on California faults. Solutions are produced for all known California faults except where noted. We focus our primary comparisons on the San Andreas Fault, which has the highest moment rate in California and the widest magnitude spectrum. We do not explicitly review the UCERF3 results, which are already fully documented (Field et al., 2014; Page et al., 2014), but we do compare three alternative model applications to the UCERF3 solutions.

3.1. Results From Integer Programming

The integer programming method is the only of the four techniques that we compare that produces true optimized results. This comes at computational cost, and requires expensive high-performance compute resources. Thus, trade-offs are necessary; the statewide integer programming solutions are conducted for 4-kyr periods, much shorter than 100 kyr used for the stress-based and greedy-sequential methods, and faults with less than 3-mm/year slip rates are omitted. Statewide a values were corrected for the moment implied by sub-3-mm/year faults. Rates for $M \geq 6.0$ earthquakes are calculated. An example slip rate fit to the San Andreas Fault is shown in Figure 5.

Given that there is one true optimal solution for a set of parameters, there might be only one integer programming result to discuss. However, since 4-kyr periods are calculated, there is variability in the input rupture sets, which are sampled at random from a Gutenberg-Richter distribution extrapolated from the preferred $M = 5.0$ statewide earthquake rate calculated by Felzer (2013b). This variability is especially evident at the highest and lowest magnitudes. The impact of this sampling on results is explored by calculating a set of 10 optimal solutions. All of the results are participation magnitude-frequency distributions because the method does not assign hypocenters. Future iterations of the method could adopt a random hypocenter assignment like that used for UCERF3 solutions.

An alternative to optimal solutions from integer programming is computing feasible solutions. A feasible solution is found by setting the objective function to zero, but retaining all of the constraints. In other words, the solution is not held to the weighted mean slip rates, but is instead constrained to fit between the minimum and maximum rates (Figure 5). This reduces the effects of strong slip rate transitions, which are difficult to match over short durations. These discontinuities are an artifact of sectioning the San Andreas Fault, and extending geologic point observations across whole sections; strong weighting of these geologic measures in UCERF3 versus GPS-based slip rates that allow for more transitional slip rate variation (Parsons et al., 2013) led to the abrupt transitions shown in Figure 5. Optimal solutions from integer programming tend to fill these sections with larger earthquakes, whereas feasible solutions allow more of the statewide budget of $M < 7$

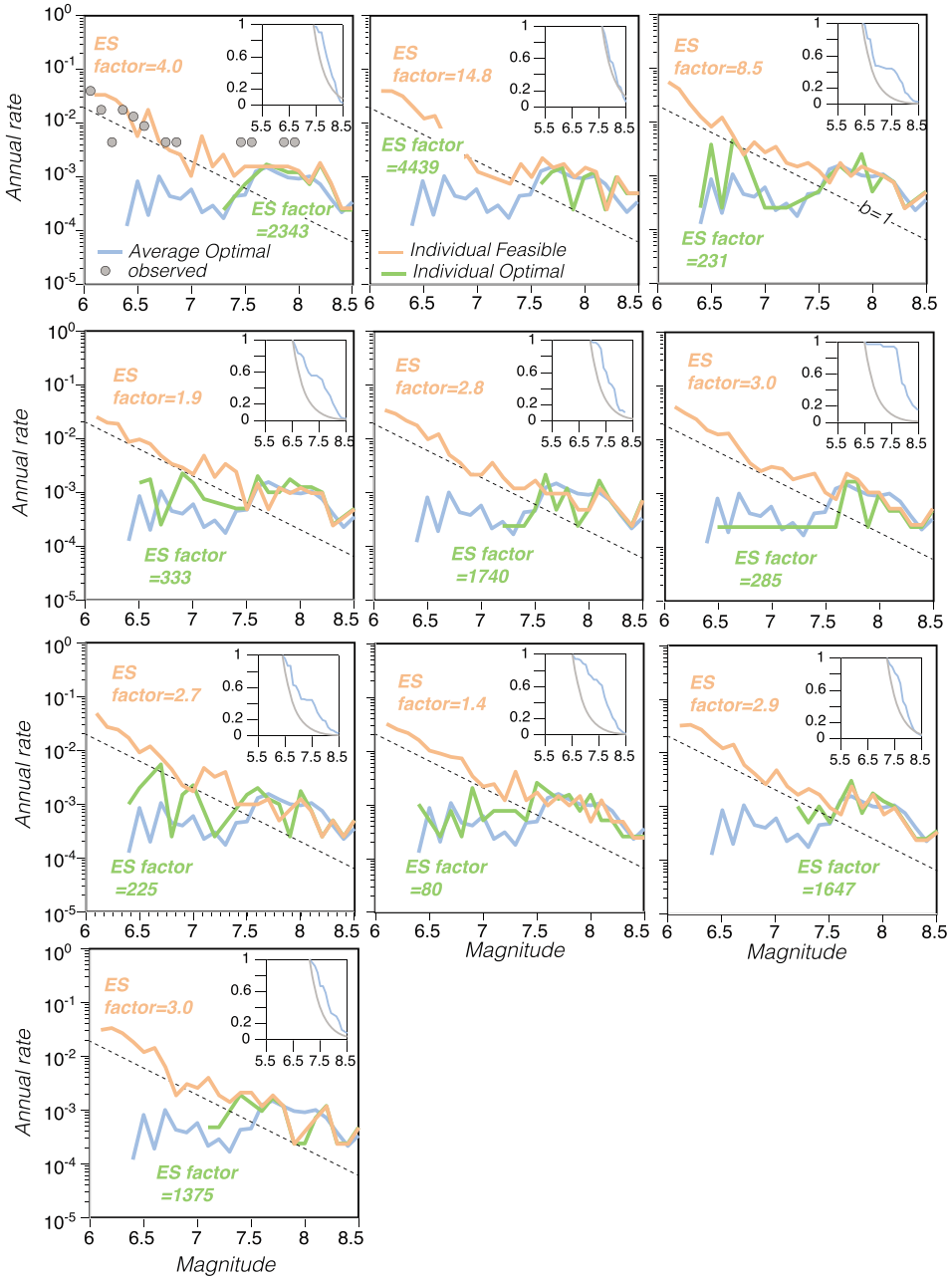

Figure 6. Incremental magnitude frequency distributions for the San Andreas Fault from 10 optimized and 10 feasible solutions using integer programming. The differences between the panels come from random sampling of 4-kyr catalogs from a continuous distribution defined by the overall statewide Gutenberg-Richter magnitude frequency distribution constrained by the observed long-term earthquake rate. Green curves are outputs from the optimal solutions, the light blue curve is the average of all 10 optimal solutions, and the orange curves are feasible solutions given the constraints. The dashed black line is an incremental $b = 1$ Gutenberg-Richter line calibrated to the observed rate of $M \geq 5.5$ earthquakes within ±5 km of the San Andreas Fault (catalog from Felzer, 2013a). Insets show empirical cumulative magnitude frequency distributions plotted with Gutenberg-Richter $b = 1$ curves that they are compared with in statistical tests (linear axes). All of the distributions are strongly characteristic with p values ~0. The ES factor values (ratio of W_2 statistic to critical value) are given for each model. The feasible solutions are all much closer to a Gutenberg-Richter form than are the optimal solutions.

earthquakes to locate along the San Andreas Fault because the fits to sharp slip rate transitions are relaxed (Figure 5).

We show 10 optimal and 10 feasible solutions for the San Andreas Fault produced by integer programming in Figure 6 to illustrate how the magnitude frequency distribution shapes are sensitive to the random sampling used to build the input catalogs. We find that the optimal solutions are the most characteristic of any of the

Table 1
Results of Comparing Calculated Magnitude-Frequency Distributions on the San Andreas Fault to a Gutenberg-Richter Distribution Using Three Statistical Methods, Kolmogorov–Smirnov Tests, Wilcoxon Rank-Sum Tests, and Epps-Singleton Tests

Model	N	Kolmogorov–Smirnov D	KS p	Wilcoxon Rank-Sum |Z|	W r-s p	Epps-Singleton W_2	ES p	ES factor	M
Nucleation magnitude-frequency									
Stress AR = 0.5, SR = 200	25,280	0.026	0.00	0.3	0.79	25.6	0.00	2.7	7.5
Greedy Hayward	1,313	0.048	0.00	2.8	0.00	41.0	0.00	4.3	8.0
Greedy San Gregorio	1,059	0.060	0.00	3.1	0.00	42.6	0.00	4.5	7.7
Greedy Garlock	973	0.133	0.00	7.8	0.00	111.5	0.00	11.8	7.6
Stress AR = 0.3, SR = 200	35,053	0.063	0.00	8.7	0.00	112.2	0.00	11.8	6.4
Stress AR = 0.8, SR = 300	14,303	0.042	0.00	1.8	0.07	122.2	0.00	12.9	7.2
Stress AR = 0.8, SR = 1,000	14,066	0.042	0.00	2.6	0.01	122.7	0.00	12.9	7.4
Stress AR = 1.0, SR = 300	10,296	0.066	0.00	2.3	0.02	262.4	0.00	27.7	7.5
Stress AR = 1.0, SR = 1,000	9,862	0.068	0.00	2.7	0.01	267.0	0.00	28.1	7.5
Stress AR = 1.0, SR = 200	9,932	0.071	0.00	2.8	0.00	295.2	0.00	31.1	7.5
Greedy bg M_{max} = 8.5, min SAF slip	7,575	0.076	0.00	4.9	0.00	296.9	0.00	31.3	7.7
Greedy bg M_{max} = 8.5	7,768	0.084	0.00	5.0	0.00	341.2	0.00	36.0	7.0
Greedy all EQ's on faults, no bg	9,154	0.097	0.00	9.6	0.00	442.9	0.00	46.7	7.7
Greedy M_{max} = 8.2	5,962	0.126	0.00	14.9	0.00	480.7	0.00	50.7	7.7
Greedy M_{max} = 8.0	6,472	0.117	0.00	11.2	0.00	507.0	0.00	53.4	7.7
Greedy min SAF slip rate	4,922	0.138	0.00	11.0	0.00	540.2	0.00	56.9	7.7
Greedy M_{max} = 8.5 alt 4	4,969	0.155	0.00	12.7	0.00	643.4	0.00	67.8	7.7
Greedy M_{max} = 8.5 alt 1	5,086	0.152	0.00	15.2	0.00	645.0	0.00	68.0	7.7
UCERF3	5,088	0.152	0.00	15.2	0.00	646.1	0.00	68.1	7.7
Greedy M_{max} = 8.5 alt 7	5,059	0.149	0.00	12.4	0.00	652.4	0.00	68.8	7.7
Greedy high *a* value	19,935	0.084	0.00	4.5	0.00	658.0	0.00	69.3	7.6
Greedy M_{max} = 8.5 alt 5	4,911	0.157	0.00	13.7	0.00	658.6	0.00	69.4	7.7
Greedy M_{max} = 8.5 alt 3	5,021	0.155	0.00	11.8	0.00	662.3	0.00	69.8	7.7
Greedy M_{max} = 8.5 alt 2	5,041	0.156	0.00	14.3	0.00	664.0	0.00	70.0	7.8
Greedy M_{max} = 8.5 alt 8	4,946	0.161	0.00	14.3	0.00	691.8	0.00	72.9	7.8
Greedy M_{max} = 8.5 alt 9	5,112	0.156	0.00	12.3	0.00	692.6	0.00	73.0	7.7
Greedy no rupture jumping	5,013	0.157	0.00	8.8	0.00	704.0	0.00	74.2	7.7
Greedy M_{max} = 8.5 alt 6	4,796	0.170	0.00	16.0	0.00	709.8	0.00	74.8	7.7
No greedy, random selection	8,565	0.123	0.00	10.6	0.00	717.7	0.00	75.6	7.6
Greedy M_{max} = 8.5 alt 10	5,006	0.163	0.00	14.2	0.00	721.6	0.00	76.1	7.7
Greedy high slip rate SAF	5,282	0.170	0.00	13.9	0.00	807.6	0.00	85.1	7.7
Stress AR = 0.2, SR = 200	44,884	0.210	0.00	32.0	0.00	1,054.5	0.00	111.1	6.4
Participation magnitude-frequency									
Integer Prog. Feasible soln. 8	633	0.043	0.25	0.3	0.79	13.1	0.01	1.4	6.4
Integer Prog. Feasible soln. 4	517	0.084	0.00	1.8	0.08	18.5	0.00	1.9	7.0
Integer Prog. Feasible soln. 7	706	0.093	0.00	3.4	0.00	26.0	0.00	2.7	6.4
Integer Prog. Feasible soln. 5	646	0.080	0.00	1.9	0.05	27.0	0.00	2.8	6.4
Integer Prog. Feasible soln. 9	722	0.053	0.06	0.3	0.80	27.2	0.00	2.9	6.5
Integer Prog. Feasible soln. 6	663	0.067	0.01	1.7	0.09	28.7	0.00	3.0	6.7
Integer Prog. Feasible soln. 10	723	0.063	0.01	0.7	0.51	28.9	0.00	3.0	6.5
Integer Prog. Feasible soln. 1	656	0.072	0.01	0.3	0.79	37.9	0.00	4.0	6.4
Integer Prog. Feasible soln. 3	743	0.168	0.00	6.8	0.00	80.9	0.00	8.5	6.4
Integer Prog. Feasible soln. 2	736	0.133	0.00	4.4	0.00	140.6	0.00	14.8	6.7
Integer Prog. All Feasible soln. Combined	7,368	0.068	0.00	3.7	0.00	156.6	0.00	16.5	6.4
Greedy bg M_{max} = 8.5	16,631	0.094	0.00	6.4	0.00	273.5	0.00	28.8	7.1
Greedy M_{max} = 8.0	12,492	0.133	0.00	13.8	0.00	397.3	0.00	41.9	7.6
Greedy bg M_{max} = 8.5, min SAF slip	13,157	0.123	0.00	12.2	0.00	402.4	0.00	42.4	6.8
Greedy all EQ's on faults, no bg	33,125	0.145	0.00	19.6	0.00	577.9	0.00	60.9	6.0
Greedy M_{max} = 8.2	13,638	0.123	0.00	10.2	0.00	633.3	0.00	66.7	7.7
No greedy, random selection	14,149	0.096	0.00	11.0	0.00	635.6	0.00	67.0	8.0
UCERF3	10,981	0.122	0.00	4.7	0.00	672.3	0.00	70.9	6.7
Integer Prog. Oprtimal soln. 8	71	0.759	0.00	12.5	0.00	758.1	0.00	79.9	6.9
Greedy M_{max} = 8.5 alt 2	7,866	0.172	0.00	19.8	0.00	763.2	0.00	80.4	7.6
Greedy high slip rate SAF	9,797	0.221	0.00	25.7	0.00	1,197.6	0.00	126.2	6.6
Greedy M_{max} = 8.5 alt 1	9,285	0.179	0.00	28.0	0.00	1,207.7	0.00	127.3	7.7
Greedy no rupture jumping	8,772	0.205	0.00	22.0	0.00	1,299.1	0.00	136.9	7.7

Table 1
(continued)

Model	N	Kolmogorov–Smirnov D	KS p	Wilcoxon Rank-Sum |Z|	W r-s p	Epps-Singleton W_2	ES p	ES factor	M
Greedy M_{max} = 8.5 alt 3	9,412	0.195	0.00	21.7	0.00	1,316.3	0.00	138.7	7.7
Greedy min SAF slip rate	31,280	0.153	0.00	19.9	0.00	1,319.2	0.00	139.0	7.6
Greedy M_{max} = 8.5 alt 10	9,310	0.231	0.00	27.1	0.00	1,375.9	0.00	145.0	7.7
Greedy M_{max} = 8.5 alt 7	9,146	0.214	0.00	23.6	0.00	1,388.7	0.00	146.4	7.6
Greedy M_{max} = 8.5 alt 9	9,496	0.199	0.00	23.5	0.00	1,397.9	0.00	147.3	7.7
Greedy M_{max} = 8.5 alt 4	9,414	0.237	0.00	27.2	0.00	1,421.9	0.00	149.9	6.6
Greedy M_{max} = 8.5 alt 5	8,784	0.235	0.00	25.8	0.00	1,456.0	0.00	153.5	7.7
Greedy M_{max} = 8.5 alt 8	8,631	0.219	0.00	26.2	0.00	1,465.7	0.00	154.5	7.6
Greedy M_{max} = 8.5 alt 6	8,341	0.224	0.00	26.9	0.00	1,491.4	0.00	157.2	7.7
Integer Prog. Oprtimal soln. 7	93	0.637	0.00	12.2	0.00	2,130.4	0.00	224.5	6.8
Integer Prog. Oprtimal soln. 3	89	0.601	0.00	11.5	0.00	2,194.2	0.00	231.3	6.6
Integer Prog. Oprtimal soln. 6	34	0.920	0.00	9.5	0.00	2,703.5	0.00	284.9	6.9
Integer Prog. Oprtimal soln. 4	80	0.664	0.00	12.5	0.00	3,157.1	0.00	332.7	6.8
Integer Prog. All Optimal soln. combined	578	0.692	0.00	34.0	0.00	5,800.0	0.00	611.3	7.6
Integer Prog. Oprtimal soln. 10	49	0.916	0.00	11.4	0.00	13,046.1	0.00	1,375.0	7.5
Integer Prog. Oprtimal soln. 9	55	0.933	0.00	12.2	0.00	15,628.6	0.00	1,647.2	7.6
Integer Prog. Oprtimal soln. 5	39	0.938	0.00	10.4	0.00	17,020.2	0.00	1,793.9	7.3
Integer Prog. Oprtimal soln. 1	43	0.948	0.00	11.0	0.00	22,226.0	0.00	2,342.5	7.6
Integer Prog. Oprtimal soln. 2	34	0.980	0.00	9.8	0.00	42,115.1	0.00	4,438.8	7.7

Note. We report the sample size for each catalog, test statistics, and resulting *p* values from each method (all <0.05). The upper part of the table shows nucleation magnitude-frequency results and the lower part participation. The test statistics from the three methods are correlated as demonstrated in Figure 4. The different model calculations are ranked by the Epps-Singleton W_2 statistic from smallest (least characteristic) to largest (most characteristic). We give the W_2 values as a ratio to the critical value (ES factor) that would correspond to a *p* value of 0.05 here and in Figures 6, 8, and 10. The last column (*M*) gives the magnitude where the greatest differences between calculated magnitude-frequency distributions and a Gutenberg-Richter distribution occur.

participation magnitude-frequency distributions we calculate from any method (ranked in Table 1). In contrast, the feasible solutions are the closest to Gutenberg-Richter of any of our participation solutions. As the difference is a result of how closely matched the solution is to the weighted mean slip rate, then it illustrates the importance of slip rate transitions inherited from a sectioned fault model.

3.2. Results From a Stress-Based Earthquake Simulator

Our stress-based earthquake simulator produces long-term $M \geq 5.0$ earthquake rates over a 100-kyr duration for all mapped California faults. The overall earthquake budget is fixed to the preferred rate calculated by Felzer (2013b), and ruptures are allowed to jump across gaps up to 5 km as in the UCERF3 calculations (Biasi et al., 2013). Rupture propagation, branching, and jumping are all controlled by back slip and interaction stresses along with two balancing parameters, a strength reduction factor that encourages rupture growth, and an aspect ratio parameter that prevents runaway ruptures. Stress parameters result from input slip rates (Parsons et al., 2013) and fault geometry (Dawson, 2013), which means that the fit to UCERF3 slip rates is very close (Figure 7). We systematically vary strength reduction and aspect ratio to gauge sensitivity of results.

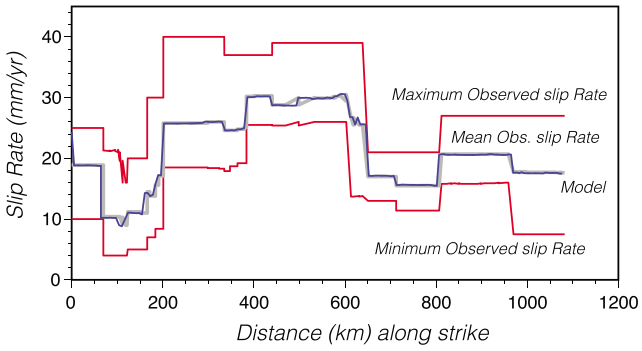

Figure 7. Slip rate fits from a stress-based simulator model are shown along strike of the San Andreas Fault. The red lines bracket the minimum and maximum UCERF3 slip rates, the gray line is the weighted mean UCERF3 slip rate, and the blue line is the model calculated slip rate.

Calculated nucleation magnitude frequency distributions on the San Andreas Fault from eight different parameter combinations are shown in Figure 8 that cover the full solution range. Differences result from parameter choices, but the overall shapes of the magnitude frequency distributions are similar. The curves approximately parallel a $b = 1$ Gutenberg-Richter line up to M~7–7.5 and then they depart from that trend with higher rates up to M~8 (Figure 8). All of the

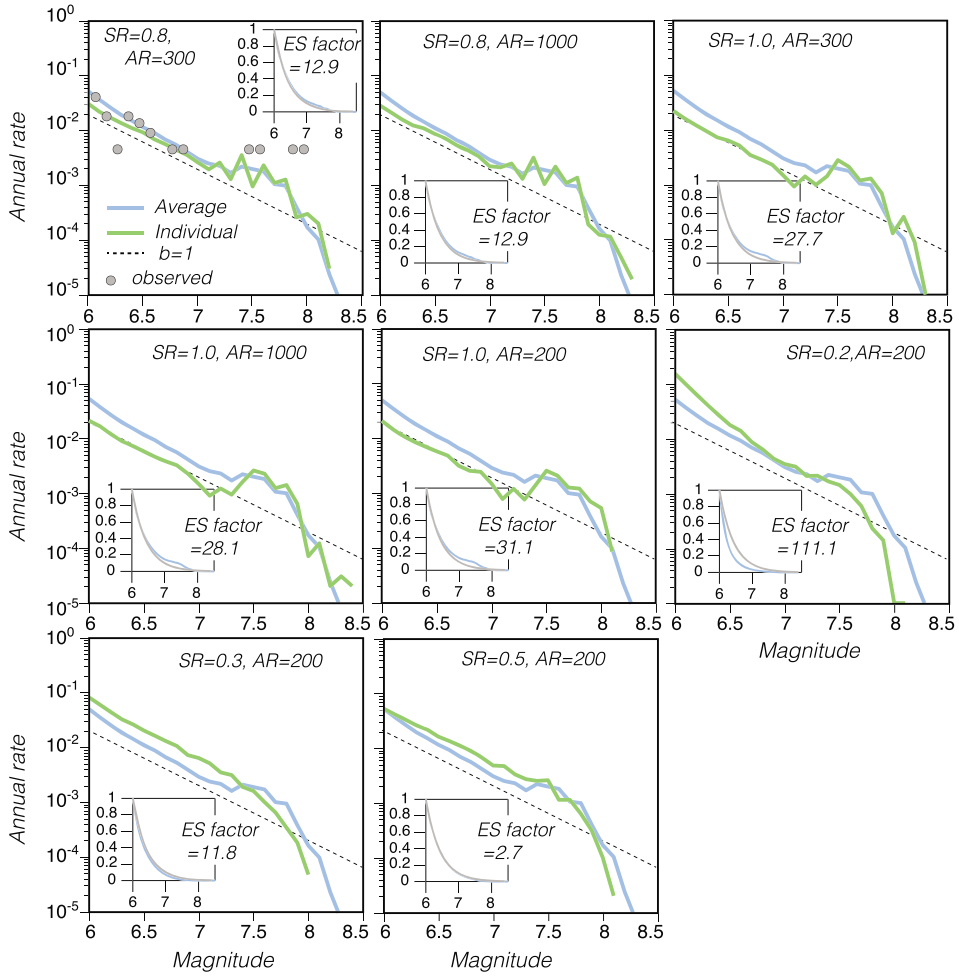

Figure 8. Incremental magnitude frequency distributions for the San Andreas Fault from 10 input parameter combinations for a stress-based simulator model. The differences between the panels result from varying two key input parameters, strength reduction (SR), which allows ruptures to grow, and the aspect ratio parameter (AR), which prevents ruptures from running away in only one direction. Green curves are model outputs, and the blue curve is the average of all solutions. The dashed black line is an incremental $b = 1$ Gutenberg-Richter line calibrated to the observed rate of $M \geq 5.5$ earthquakes within ±5 km of the San Andreas Fault (catalog from Felzer 2013a). Insets show normalized cumulative magnitude frequency distributions plotted with Gutenberg-Richter $b = 1$ curves that are compared with in statistical tests (linear axes), and corresponding *ES factor* values (ratio of Epps-Singleton W_2 statistic to critical value for p value = 0.05).

solutions can be rejected as being consistent with a Gutenberg-Richter form with p values ~0.0 from all three statistical tests we apply (Table 1), with two exceptions that have p values >0.05 from the Wilcoxon rank-sum test only (Table 1).

The aspect ratio parameter has the most influence on the maximum earthquake size in the simulations, ranging between M~8.0 and the maximum possible earthquake in the fault model at M~8.5, which represents a complete rupture of the San Andreas and connected Mendocino Faults. Most of the stress simulator solutions have more small to moderate earthquakes than observed for the San Andreas Fault (Figure 8), which may result from interaction stress increases that represent aftershocks that may not be fully accounted for in the ~150-year historic catalog. The maximum difference between the calculated magnitude distributions and Gutenberg-Richter distributions occurs between $M = 7.2$ and $M = 7.6$ for most solutions (Table 1).

3.3. Results From a Greedy Sequential Model

We use this simple method primarily to test sensitivity to data choices/parameters. It is not computationally expensive in the sense that it does not require large amounts of memory in high-performance computer resources. These features enable comprehensive sensitivity testing of results to many of the UCERF3 consensus decisions regarding rupture processes and the earthquake distribution. For example, we vary the

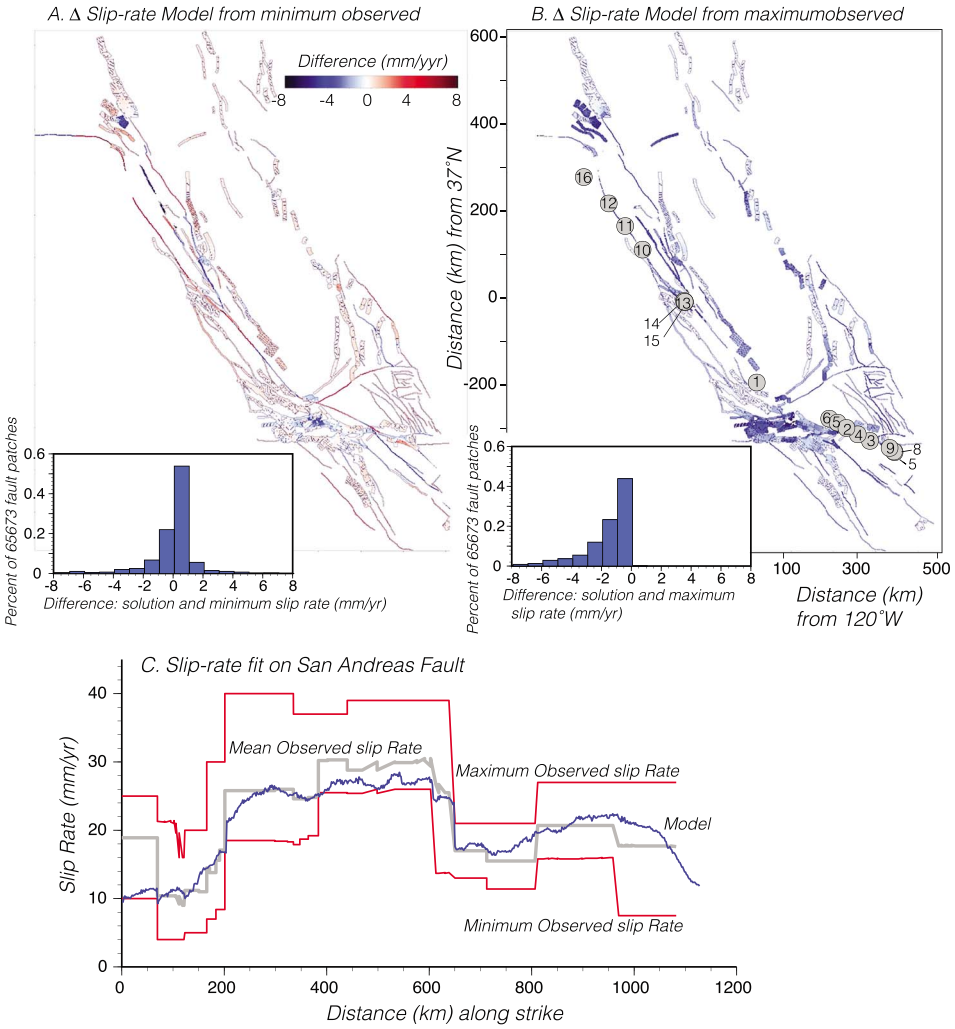

Figure 9. Slip rate fitting. (a) The difference in mm/year between the greedy sequential model and minimum UCERF3 slip rates on all California faults is shown. Red shading means slip rates above the minimum, and faults with blue shading are places that the method could not be fit to at least the minimum rate. The inset histogram shows the number of fault sections (UCERF3 designations) that have solutions above or below the minimum rate. (b) The same calculations are shown except for the UCERF3 maximum rate. Numbered circles show the locations of San Andreas Fault paleoseismic sites. No calculated rates exceeded the maximum UCERF3 rates. (c) The slip rate fits are shown along strike of the San Andreas Fault. The red lines bracket the minimum and maximum UCERF3 slip rates, the gray line is the weighted mean UCERF3 slip rate, and the blue line is the model calculated slip rate.

maximum magnitude threshold on faults, and the maximum magnitude threshold in the background. We run simulations with background moment rates equal to UCERF3 (~16%) as well as those with no background events, we test the preferred and maximum statewide *a* values (Felzer, 2013b), we allow ruptures to jump across 5-km gaps, and we run models that disallow all rupture jumping. We additionally test the effect of the greedy sequential algorithm versus purely random (nonsequential) earthquake sequences.

3.3.1. Slip Rate Fit

An example slip rate fit to all California faults and a detail of the San Andreas Fault is shown in Figure 9. In general, the method has difficulty matching all slip rate observations because the fault model implies an annual moment rate of ~2.8E + 19 Nm/year, whereas the sum of the available earthquakes assigned to faults yields an average annual rate of 1.8E + 19 Nm/year if 16% of the moment is in the background (Field et al., 2014) and the maximum magnitude of background events is M = 7.6. The essentially unknown influences of variable fault coupling and aseismic deformation from brittle creep are significant sources of uncertainty in moment-balanced solutions. We adopt the UCERF3 90% coupling coefficients on faults, as well as the aseismicity factor values on creeping faults (Field et al., 2014).

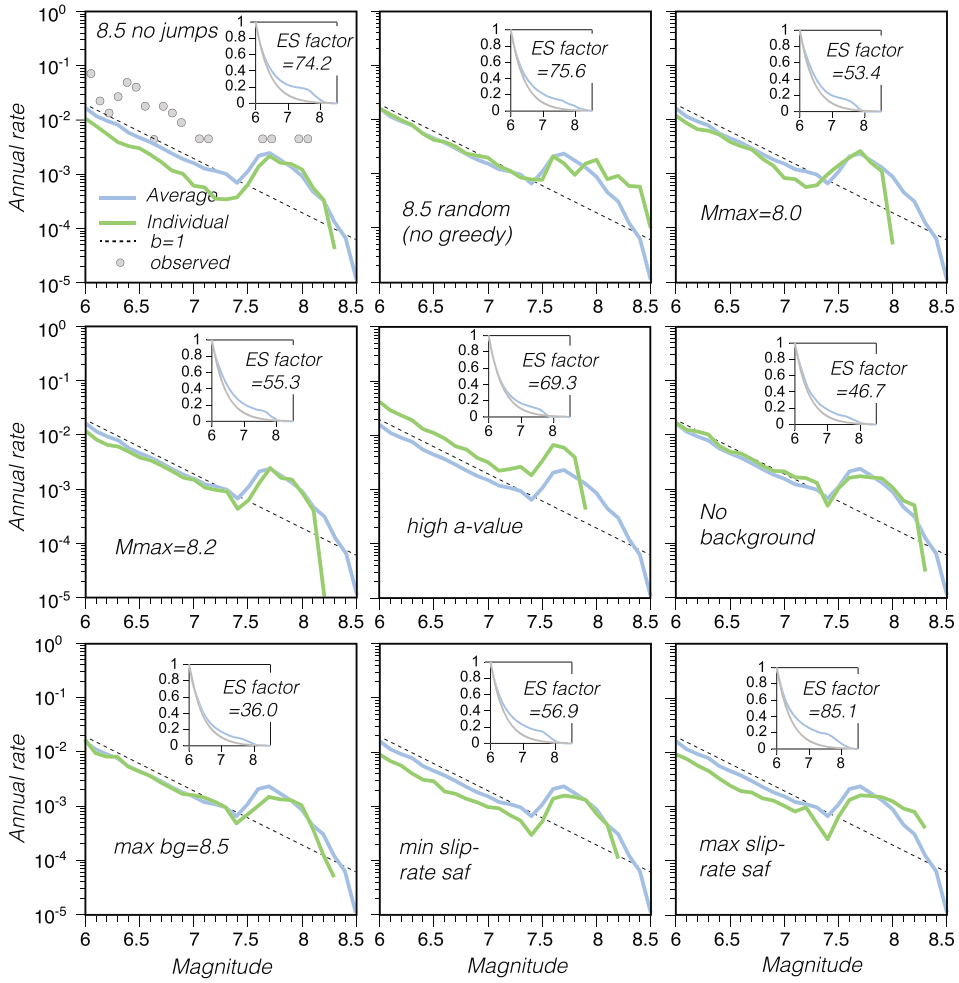

Figure 10. Incremental nucleation magnitude frequency distributions for the San Andreas Fault from nine data parameter combinations for a greedy sequential model. The differences between the panels result from varying data parameters. These include not allowing earthquake ruptures to jump across gaps, setting different maximum magnitudes allowed (M = 8.0–8.5), using a random magnitude assignment instead of the greedy algorithm, using the highest possible California earthquake rate instead of the UCERF3 preferred rate (Felzer, 2013b), altering the maximum background earthquake magnitude from zero to M = 8.5, and fitting the highest and lowest allowable San Andreas slip rates. Blue curves are model outputs, and the green curve is the average of all solutions. The dashed black line is an incremental b = 1 Gutenberg-Richter line calibrated to the observed rate of $M \geq 5.5$ earthquakes within ±5 km of the San Andreas Fault (catalog from Felzer 2013a). Insets show empirical distribution functions plotted with Gutenberg-Richter b = 1 curves they are compared with in statistical tests (linear axes), and corresponding *ES factor* values (ratio of Epps-Singleton W_2 statistic to critical value for p value = 0.05).

3.3.2. Magnitude Frequency Distribution on the San Andreas Fault

Results from parameter sensitivity tests are summarized in Figure 10, where the calculated San Andreas Fault nucleation magnitude frequency distributions generated from a variety of inputs are shown. The curves tend to parallel the Gutenberg-Richter slope up to M~7.5, above which there appear to be more high-magnitude events than would be predicted from a strict exponential trend (Figure 10). These solutions are all consistent with a characteristic magnitude-frequency distribution model, with three statistical methods ruling out a Gutenberg-Richter model (Table 1 and Figure 10). There is an additional component of variation associated with the method because each run assigns initial hypocenters at random. Thus, no two results with the same data parameters are identical. We show the results for San Andreas Fault magnitude frequency distributions for ten runs that use the same data parameters (highest weighted values from UCERF3) to demonstrate the effects of this randomization (Figure 11).

Varying data inputs and the resulting degree of how characteristic the resulting magnitude-frequency distributions lend some insight into which data constraints may be driving the results. We find that the parameter change that most influences the solutions to be less characteristic involves the maximum magnitude of

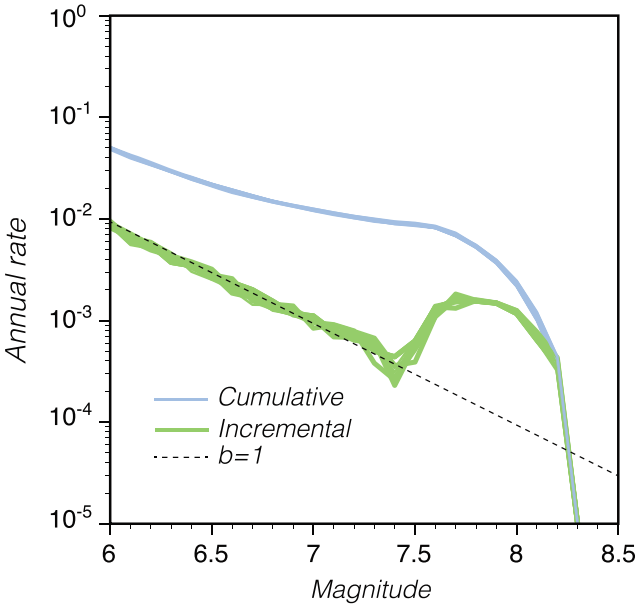

Figure 11. Nucleation magnitude frequency solution variability with input parameters fixed (preferred UCERF3 *a* value (Felzer, 2013b), preferred M_{max} = 7.6 of background earthquakes, and rupture jumping distance of 5 km (Field et al., 2014)). The green curves show incremental variation on the San Andreas Fault from ten different runs due to the random location assignments inherent to the algorithm, and the blue lines show the cumulative curves.

earthquakes that are allowed to occur off of known faults (background events). The greedy solution that is the least characteristic based on ranking by the Epps-Singleton W_2 statistic is one that allows earthquakes up to the maximum magnitude (M = 8.5) to occur off of known faults, and that fits San Andreas Fault slip rates from geodetic values, which are slower than the consensus mean that includes geologic offset data (Table 1). The next least characteristic solution after that has high background magnitudes and a fit to the consensus mean. By putting more high magnitudes into the background, the San Andreas Fault has a smaller characteristic "bump" above M~7.5. The UCERF3 consensus view was that $M > 7.6$ earthquakes could not have happened in California off-mapped faults without leaving clear signs on the landscape. The most characteristic solutions from the greedy algorithm are found when the faults are not allowed to connect by rupture jumping when end points are within 5 km of each other. Solutions using the UCERF3 consensus parameters, with the overall maximum magnitude of M = 8.5, and a background maximum magnitude of M = 7.6 tend to also be among the most characteristic results (Table 1).

3.3.3. Fit to Paleoseismic Data

The UCERF3 earthquake rate inversions were directly constrained by paleoseismic observations (Field et al., 2014). In our simulations we reserve the paleoseismic observations for testing. Example calculated magnitude frequency distributions are plotted in Figure 12 with the mean and ±1σ rates (dashed lines) from San Andreas paleoseismic sites (Parsons, 2012; Weldon, Schmidt, et al., 2013). Fitting these observations depends on the magnitudes of the events identified in the paleoseismic observations. We use the calculated participation magnitude-frequency distributions from the greedy sequential algorithm at each section where paleoseismic data are observed to find the predicted magnitudes at paleoseismic sites (Figure 12); the mean paleoseismic rates and 1σ uncertainties identify the ranges that paleomagnitudes would have to be to fit the calculated rates (heavy red lines on Figure 12). We compare theses predicted magnitude ranges to those calculated from mean paleodisplacements by Weldon, Schmidt, et al. (2013; dark gray dots on Figure 12) by applying the same moment magnitude relation of Hanks and Kanamori (1979) that we used to translate magnitudes to average slip in the greedy sequential algorithm as

$$\frac{\bar{s} = 10^{(1.5M_w + 9.05)})}{\mu A.}$$

If we apply the same magnitude-area relation (Ellsworth B; $M_w = \log(A) + 4.2$) [WGCEP (Working Group on California Earthquake Probabilities), 2003] as used in rate calculations and assume that observed paleoslip is equal to the average slip, then the paleomagnitude is $M_w = 2\log(\bar{s}\mu) - 26.5$, where μ = 30 GPa.

The average paleomagnitudes fall outside of the ±1σ range from predicted values on three San Andreas Fault sections (San Bernardino, Carrizo, and Santa Cruz Mountains; Figure 12), which implies a mismatch to those data. The range of paleo offsets is not given in the Weldon, Schmidt, et al. (2013) report, so we do not know what the breadth of, or minimum thresholds of observation are at those sites. In all the misfit cases the paleomagnitudes are higher than the corresponding rate calculations, which imply that we may underestimate high magnitude rates on some San Andreas sections.

3.3.4. Magnitude Frequency Distributions on Other Faults

Long faults with the highest slip rates have the most earthquakes across the widest magnitude spectrum, and they thus offer the largest rate samples for solutions calculated over fixed periods. We therefore examine three long, connected fault systems to broaden our analysis from the San Andreas Fault: the Garlock Fault, the San Gregorio/Hosgri fault system, and the Hayward/Rodgers Creek/Calaveras system (Figure 13). Ten calculations are made for nucleation magnitude frequency using the greedy sequential model with the same parameters for each fault system (preferred UCERF3 *a* value (Felzer, 2013b),

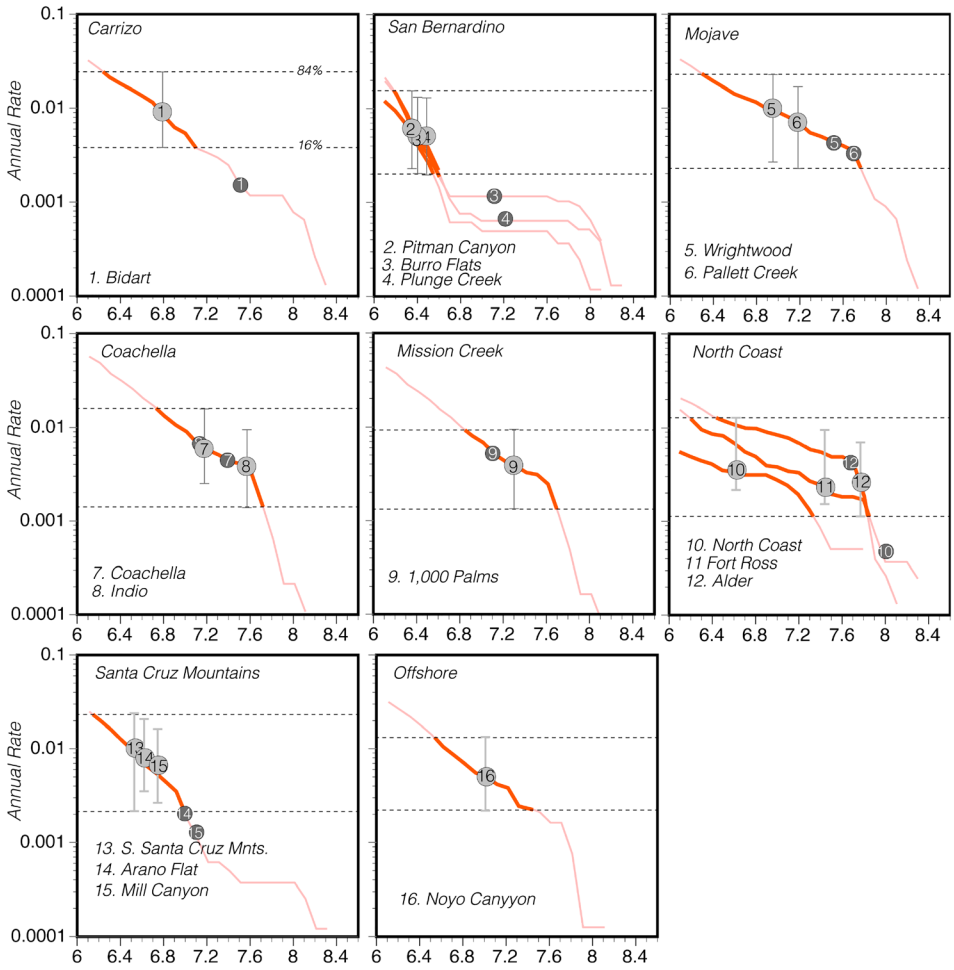

Figure 12. Observed earthquake rates from paleoseismic studies (light gray dots; Weldon, Schmidt, et al., 2013) shown with calculated magnitude frequency rates on the San Andreas Fault. Paleorates are not associated with magnitudes; we fit them within ±1σ uncertainties to the calculated magnitude frequency distributions at each site (red curves), which yields the implied minimum and maximum paleomagnitudes (heavy red lines). Locations of paleosites are shown in Figure 9. The model is compatible with paleoseismic rates depending on the minimum magnitude of detection, which would have to range between M = 6.4 and M = 7.6, depending on the site. Dark gray dots show magnitudes calculated from mean observed paleo offsets where available (Weldon, Schmidt, et al., 2013), which in some cases fall outside the ±1σ error bar ranges calculated by Parsons (2012), implying a misfit to the paleodata at those sites.

preferred M_{max} = 7.6 of background earthquakes, and rupture jumping distance of 5 km (Field et al., 2014)).

The magnitude frequency distributions on these three faults show more variability between runs as compared with the San Andreas Fault results because the slip rates are lower, and thus, there are fewer earthquakes per 100 kyr. However, their average distributions are similar in shape to the San Andreas solutions from multiple methods; they tend to parallel a Gutenberg-Richter trend, and then have elevated rates at higher magnitudes (Figure 13). A Gutenberg-Richter distribution can be ruled out for all of our solutions using three statistical methods (Table 1). The Epps-Singleton factor is shown for each fault in Figure 13, which range between 4.3 and 11.8 with a value needed less than 1 to have a 5% chance of being Gutenberg-Richter. Thus, our results show consistent characteristic nucleation magnitude-frequency distributions on major California fault lines.

4. Discussion and Conclusions

Our goal for this exercise is to determine if a quality set of consensus data informing four different earthquake rate calculation methods can produce a definitive answer about magnitude frequency distributions on

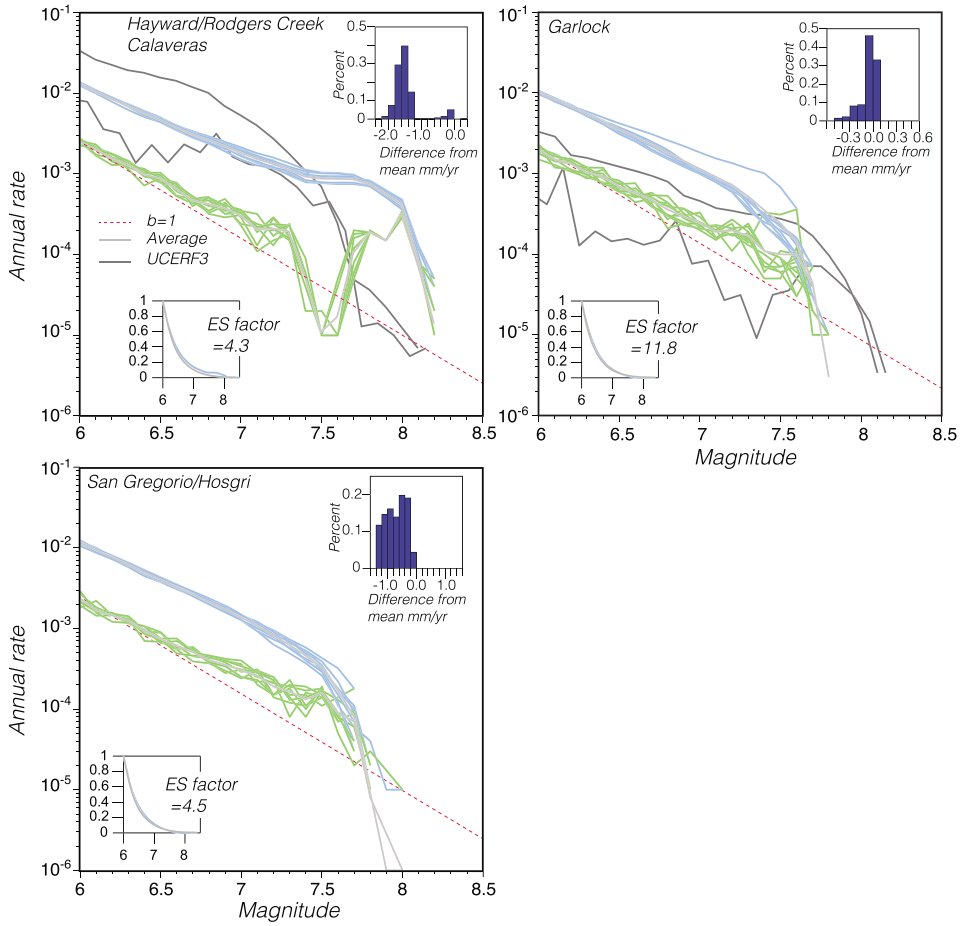

Figure 13. Nucleation magnitude frequency distributions calculated with the greedy sequential model for three connected fault systems. Incremental curves are shown in green, and cumulative in blue. Ten realizations using the same parameters are shown (preferred UCERF3 *a* value (Felzer, 2013b), preferred M_{max} = 7.6 of background earthquakes, and rupture jumping distance of 5 km (Field et al., 2014)). Inset histograms show the distribution of slip rate misfit from the mean UCERF3 rates, which generally are ~1–2 mm/year below, but fall above the minimum values (Figure 9). All of these faults have magnitude-frequency distributions that are significantly different from Gutenberg-Richter with *ES factor* values >1.0 (Table 1). UCERF3 incremental and cumulative nucleation magnitude-frequency curves are shown for reference (dark gray lines).

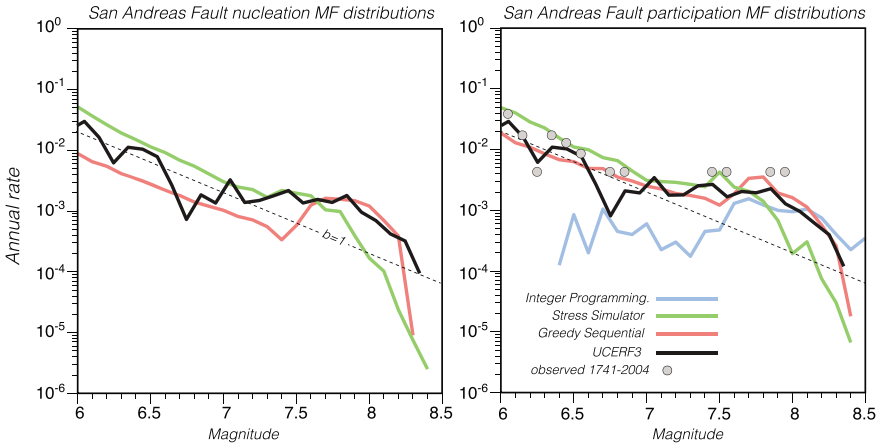

Figure 14. Four calculated incremental magnitude frequency distribution solutions averaged from multiple runs by UCERF3 (Field et al., 2014; black curve), as well as integer programming (optimal results; blue curve), stress simulator (green curve), and greedy sequential methods (red curve). Observed earthquakes (Felzer, 2013a) located within ±5 km of the San Andreas surface trace are shown by gray dots. A Gutenberg-Richter line extrapolated from the observed *M* = 5.5 rate is plotted (dashed line).

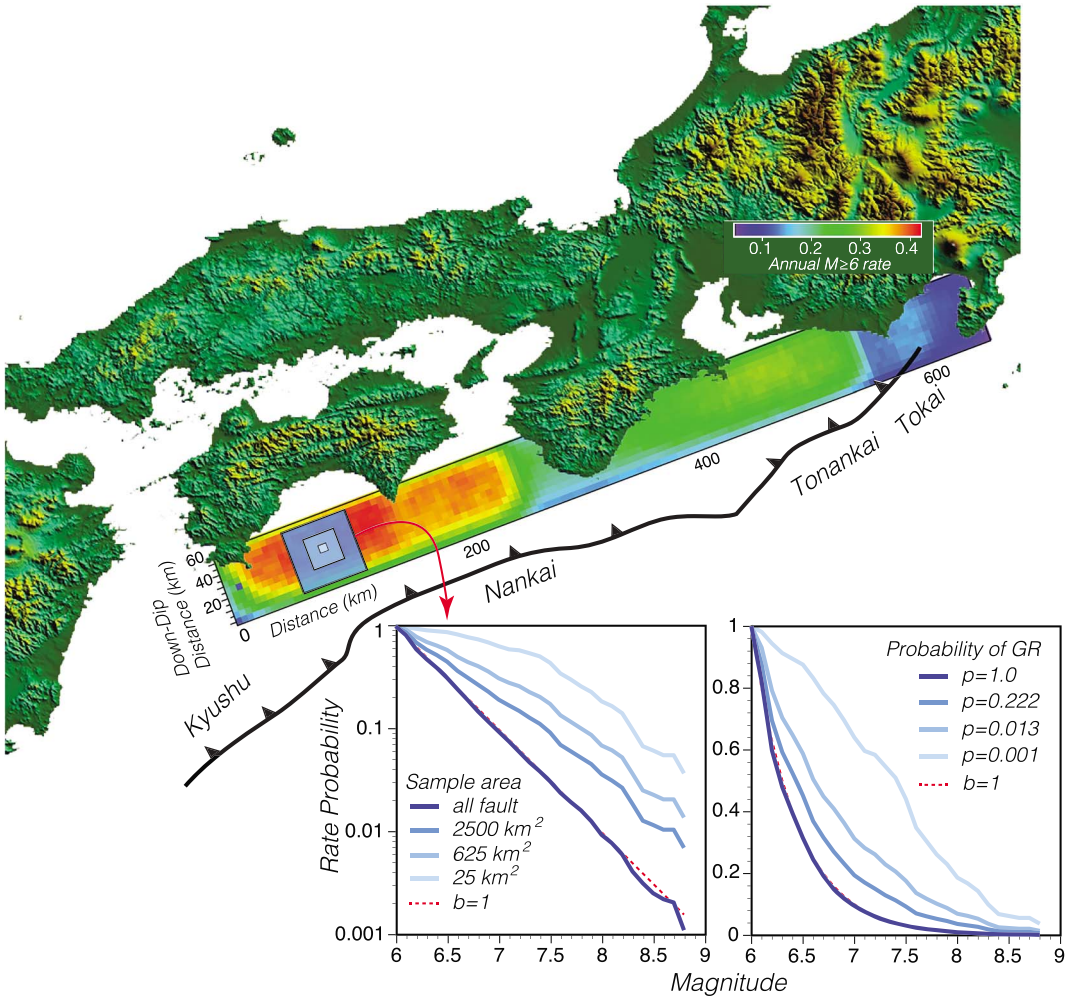

Figure 15. Testing the effects of spatial subsampling on magnitude frequency distributions. As an example, we work with a controlled simulation on the Nankai subduction zone in Japan (Parsons et al., 2012). In this instance, the magnitude-frequency distribution of a single fault is required to be fit to a b = 1 Gutenberg-Richter distribution. We subsample participation magnitude frequency on three areas of 25-, 625-, and 2,500-km^2 size, and compare with a b = 1 Gutenberg-Richter distribution. As expected the whole fault has a probability of 1.0 of being Gutenberg-Richter. This probability drops as sampling areas decrease, with the 625- and 25-km^2 samples being significantly different (p values $<$0.05).

individual faults. Generally, the preferred California a value does not yield enough cumulative moment to fully satisfy the UCERF3 slip rates on all faults in our calculations, which causes our solvers to put more high-magnitude earthquakes relative to lower on the fastest slipping faults in order to fit the slip rates. For example, the calculated average annual moment expressed along the San Andreas Fault for the four methods ranges between 2.1 and 2.9 times higher than that implied by a normalized Gutenberg-Richter distribution with b value = 1.0. This is balanced by assigning lower magnitude events into the background or on smaller, slower slipping faults. An example of this effect can be seen in the UCERF3 results shown in Figure 1, where on the North Mojave section of the San Andreas Fault, M~6.6 earthquake nucleation is 25 times less common than M~8 shocks, almost the exact inverse of the relative global occurrence rates of these magnitudes. These distributions at section scale are fairly typical of all the results. The rate differences are muted, though still quite characteristic when the entire San Andreas Fault is examined, in which case M~6.6 earthquake nucleation is expected to outnumber M~8.0 nucleation by factors between 3 and 12 depending on the method (Figure 14). We therefore conclude from three new independent analyses along with the UCERF3 calculations that faults within the interconnected system in California have characteristic earthquake nucleation with higher large-magnitude rates than would be expected from a Gutenberg-Richter distribution provided that the long-term earthquake rate is stationary and similar to that observed

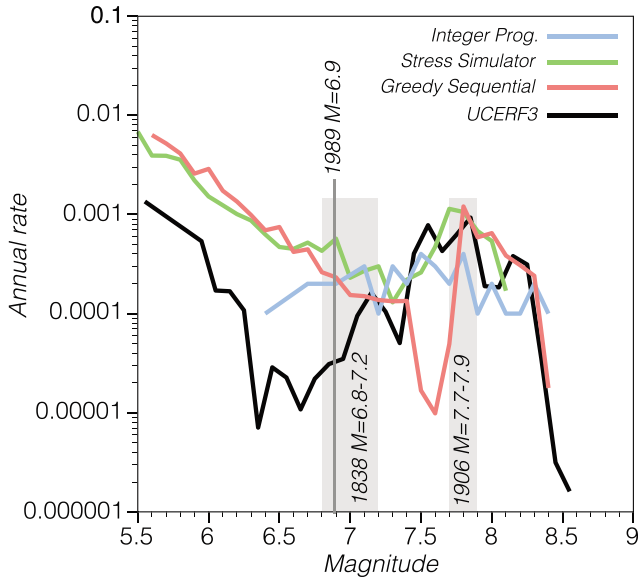

Figure 16. Four incremental magnitude frequency distributions are shown for the San Francisco peninsula section of the San Andreas Fault from four different solution methods. Three historical $M \geq 6.9$ earthquakes that involved the peninsula section are plotted for magnitude range; the heights of the bars do not imply rate values.

over the past 150 years. These results are consistent with the idea that a self-similar group of faults with characteristic magnitude distributions will yield an overall Gutenberg-Richter distribution (e.g., López-Ruiz et al., 2004).

We draw conclusions about why California faults have characteristic magnitude-frequency distributions by examining the relative departures from Gutenberg-Richter behavior of the solutions from the same method with different data input parameters. The consensus parameter set has a fast slipping San Andreas Fault, and allows only $M \leq 7.6$ earthquakes to happen away from mapped faults. These influences on solutions from the greedy algorithm, for example, mean that most of the highest-magnitude earthquakes must occur on the San Andreas and linked faults because their high moment allows the fast slip rates to be fit, and there are few other faults that can accommodate the highest-magnitude events. We find solutions that are closer to Gutenberg-Richter if these constraints are relaxed (Table 1) by allowing background earthquakes up to $M = 8.5$, reducing the overall maximum magnitude, and/or fitting the San Andreas Fault to minimum thresholds of UCERF3 slip rates.

While almost all solutions are characteristic, we note some methodological influences on the results. For nucleation magnitude frequency, the stress-based method has the smallest difference from Gutenberg-Richter with a mean Epps-Singleton W_2 parameter of 282.7 (factor of 34.0 above critical value for $p = 0.05$), followed by the greedy algorithm with a mean Epps-Singleton W_2 parameter of 540.6 (factor of 61.3 above critical value for $p = 0.05$), and then the UCERF3 result with an Epps-Singleton W_2 parameter of 646.1 (factor of 68.1 above critical value for $p = 0.05$; Table 1). Perhaps a more intuitive comparison can be made using the Kolmogorov–Smirnov D statistic, which is expressed as the maximum percentage difference in rate between the empirical distribution function and the cumulative null model (Gutenberg-Richter). In that case the mean D values for the stress-based and greedy algorithms are the same with $D = 0.130$, and the UCERF3 D value is 0.156 (Table 1). We calculate the magnitudes where the greatest differences between the calculated magnitude-frequency distributions and a Gutenberg-Richter distribution occur (listed in Table 1); the mean value for the stress-based method is $M = 7.2$, and it is $M = 7.7$ for the greedy algorithm and UCERF3 results. For participation magnitude frequency, we note strong differences between the integer programming results depending on whether optimal or feasible solutions are performed. For optimal solutions, the mean Epps-Singleton W_2 parameter is 12,602.1 (factor of 1,328.2 above critical value for $p = 0.05$), and for feasible solutions the mean Epps-Singleton W_2 parameter is 42.9 (factor of 4.5 above critical value for $p = 0.05$). The mean Kolmogorov–Smirnov D statistics are 0.823 for optimal solutions, and 0.086 for feasible (Table 1).

Test statistics thus show that the stress-based simulator results return nucleation magnitude-frequency distributions that are closer to Gutenberg-Richter than the other methods, and the integer programming feasible solutions also return participation magnitude-frequency distributions that are closer to Gutenberg-Richter than other methods. In the first case we suggest that the difference results from the stress-based method using stress interaction calculations to propagate and filter ruptures directly, whereas the other methods apply the rupture filtering rules defined by Field et al. (2014) (described in section 2.1). The differences between integer programming feasible and optimal results are caused by how strictly the solutions were fit to input slip rate discontinuities from strong weighting of geologic offset measures that were extrapolated across fault sections. We thus find that interpretive decisions about the maximum possible magnitude on and off faults, slip rate transitions, relative weighting between geodetic and geologic slip rate models, and rupture filtering all have influence on the shape of calculated magnitude distributions. However, none of these influences are strong enough to change the distribution shapes from characteristic to Gutenberg-Richter.

The participation magnitude-frequency distribution at points is most applicable to hazard calculations and is expected to be characteristic with a balance toward higher magnitudes because more large events that nucleate far away on different faults can spread onto a specific fault or fault section than can smaller ones. This is an example of spatial subsampling, something known to affect exponential distribution shapes (e.g., Priesemann et al., 2009; Levina & Priesemann, 2017). We demonstrate this effect by constructing a synthetic earthquake catalog for a single fault surface that is constrained to have Gutenberg-Richter nucleation magnitude frequency. In this example we use calculated earthquake rates on a simplified version of the Nankai subduction zone (Parsons et al., 2012), and sample areas of decreasing size for participation magnitude-frequency distributions. We find that as sample areas are reduced, their participation magnitude-frequency distributions become systematically more characteristic (Figure 15). This tendency is caused by the fact that higher-magnitude earthquakes affect larger areas of a fault, and multiple such events can overlap a sample point. It is therefore necessary to quantify the characteristic shapes of the nucleation and participation magnitude-frequency distributions at section scale or below depending on the forecast application (e.g., Field et al., 2017).

We lastly note methodological influences on participation magnitude-frequency distributions at section scale that could have hazard calculation implications. Different trade-offs are made in the magnitude rates at different levels depending on the calculation method, with the UCERF3 and integer programming solutions showing relatively low rates below M = 7.1, and the greedy algorithm having low rates between M = 7.4 and 7.7 (Figure 16). These differences arise in part because the UCERF3 inversion applies magnitude-frequency constraints based on regional seismicity rates and the on-fault UCERF2 (Field et al., 2009) distributions, whereas the alternative methods used here draw from a statewide pool of earthquakes.

Acknowledgments
We appreciate the efforts of Ned Field, Yehuda Ben-Zion, two anonymous readers, and an anonymous associate editor, whose reviews fundamentally changed this manuscript for the better. Kevin Milner graciously provided detailed results from the UCERF3 study. Data are available at http://www.wgcep.org/UCERF3.

References

Andrews, D. J., & Schwerer, E. (2000). Probability of rupture of multiple fault segments. *Bulletin of the Seismological Society of America*, *90*(6), 1498–1506. https://doi.org/10.1785/0119990163

Biasi, G. P., Parsons, T., Weldon, R. J. II, & Dawson, T. E. (2013). Appendix J—Fault-to-fault rupture probabilities, USGS Open-File Report 2013–1165, 20 pp.

Chen, D.-S., Batson, G., & Dang, Y. (2010). *Applied Integer Programming: Modeling and Simulation*, (p. 469). Hoboken, New Jersey: John Wiley & Sons.

Clauset, A., Shalizi, C. R., & Newman, M. E. J. (2009). Power-law distributions in empirical data. *SIAM Review*, *51*(4), 661–703. https://doi.org/10.1137/070710111

Console, R., Carluccio, R., Papadimitriou, E., & Karakostas, V. (2015). Synthetic earthquake catalogs simulating seismic activity in the Corinth Gulf, Greece, fault system. *Journal of Geophysical Research: Solid Earth*, *120*, 326–343. https://doi.org/10.1002/2014JB011765

Console, R., Nardi, A., Carluccio, R., Murru, M., Falcone, G., & Parsons, T. (2017). A physics-based earthquake simulator and its application to seismic hazard assessment in Calabria (southern Italy) region. *Acta Geophysica*, *65*(1), 243–257, https://doi.org/10.1007/s11600-017-0020-2.

Cormen, T. H., Leiserson, C. E., Rivest, R. L., & Stein, C. (2009). *Introduction to Algorithms*, (3rd ed.p. 1312). Cambridge, Massachusetts: MIT Press, Massachusetts Institute of Technology.

Cornell, C. A. (1968). Engineering seismic risk analysis. *Bulletin of the Seismological Society of America*, *58*, 1583–1606.

Dawson, T. E. (2013). Appendix A—Updates to the California Reference Fault Parameter Database—Uniform California Earthquake Rupture Forecast, Version 3 Fault Models 3.1 and 3.2, USGS Open-File Report 2013–1165, 18 pp.

Epps, T. W., & Singleton, K. J. (1986). An omnibus test for the two-sample problem using the empirical characteristic function. *Journal of Statistical Computation and Simulation*, *26*(3-4), 177–203. https://doi.org/10.1080/00949658608810963

Felzer, K. R. (2013a). Appendix K—The UCERF3 earthquake catalog, USGS Open-File Report 2013–1165, 5 pp.

Felzer, K. R. (2013b). Appendix L—Estimate of the seismicity rate and magnitude frequency distribution of earthquakes in California from 1850 to 2011, USGS Open-File Report 2013–1165, 13 pp.

Field, E. H., Biasi, G. P., Bird, P., Dawson, T. E., Felzer, K. R., Jackson, D. D., Johnson, K. M., et al. (2014). Uniform California Earthquake Rupture Forecast, version 3 (UCERF3)—The time-independent model. *Bulletin of the Seismological Society of America*, *104*(3), 1122–1180. https://doi.org/10.1785/0120130164

Field, E. H., Dawson, T. E., Felzer, K. R., Frankel, A. D., Gupta, V., Jordan, T. H., Parsons, T., et al. (2009). The Uniform California Earthquake Rupture Forecast, version 2 (UCERF 2). *Bulletin of the Seismological Society of America*, *99*(4), 2053–2107. https://doi.org/10.1785/0120080049.

Field, E. H., Milner, K. R., Hardebeck, J. L., Page, M. T., van der Elst, N., Jordan, T. H., Michael, A. J., et al. (2017). A spatiotemporal clustering model for the third Uniform California Earthquake Rupture Forecast (UCERF3-ETAS): Toward an operational earthquake forecast. *Bulletin of the Seismological Society of America*, *107*(3), 1049–1081. https://doi.org/10.1785/0120160173

Field, E. H., & Page, M. T. (2011). Estimating earthquake-rupture rates on a fault or fault system. *Bulletin of the Seismological Society of America*, *101*(1), 79–92. https://doi.org/10.1785/0120100004

Geist, E. L., & Parsons, T. (2014). Undersampling power law size distributions: Effect on the assessment of extreme natural hazards. *Natural Hazards*, *72*(2), 565–595. https://doi.org/10.1007/s11069-013-1024-0

Geist, E. L., & Parsons, T. (2018). Determining on-fault earthquake magnitude distributions from integer programming. *Computers and Geosciences*, *111*, 244–259. https://doi.org/10.1016/j.cageo.2017.11.018

Geller, R. J., Mulargia, F., & Stark, P. B. (2015). Why we need a new paradigm of earthquake occurrence. In G. Morra, D. A. Yuen, S. D. King, S.-M. Lee, & S. Stein (Eds.), *Subduction Dynamics: From Mantle Flow to Mega Disasters* (chap. 11, pp. 183–191). Hoboken, NJ: John Wiley & Sons, Inc. https://doi.org/10.1002/9781118888865.ch10

Goerg, S. J., & Kaiser, J. (2009). Nonparametric testing of distributions—The Epps–Singleton two-sample test using the empirical characteristic function. *The Stata Journal*, *9*, 454–465.
Gutenberg, B., & Richter, C. R. (1954). Magnitude and energy of earthquakes. *Annali di Geofisica*, *9*, 1–15.
Hanks, T. C., & Kanamori, H. (1979). A moment magnitude scale. *Journal of Geophysical Research*, *84*(B5), 2348–2350. https://doi.org/10.1029/JB084iB05p02348
Hecker, S., Abrahamson, N. A., & Wooddell, K. E. (2013). Variability of displacement at a point: Implications for earthquake-size distribution and rupture hazard on faults. *Bulletin of the Seismological Society of America*, *103*(2A), 651–674. https://doi.org/10.1785/0120120159
Ishibe, T., & Shimazaki, K. (2012). Characteristic earthquake model and seismicity around late Quaternary active faults in Japan. *Bulletin of the Seismological Society of America*, *102*(3), 1041–1058. https://doi.org/10.1785/0120100250
Ishimoto, M., & Iida, K. (1939). Observations sur les seismes enregistres par le microseimographe construit dernierement (in Japanese with French abstract). *Bulletin. Earthquake Research Institute, University of Tokyo*, *17*, 443–478.
Kagan, Y. Y., Jackson, D. D., & Geller, R. J. (2012). Characteristic earthquake model, 1884–2011, R.I.P. *Seismological Research Letters*, *83*(6), 951–953. https://doi.org/10.1785/0220120107
Klotz, E., & Newman, A. M. (2013). Practical guidelines for solving difficult mixed integer linear programs. *Surveys in Operations Research and Management Science*, *18*(1-2), 18–32. https://doi.org/10.1016/j.sorms.2012.12.001
Kolmogorov, A. N. (1933). Sulla determinazione empirica di una legge di distribuzione. *Giornale dell' Istituto Italiano degli Attuari*, *4*, 83–91.
Korte, B., & Vygen, J. (2014). *Combinatorial Optimization: Theory and Algorithms*, (5th ed.p. 660). Berlin Heidelberg: Springer.
Levina, A., & Priesemann, V. (2017). Subsampling scaling. *Nature Communications*, *8*, 15140. https://doi.org/10.1038/ncomms15140
López-Ruiz, R., Vázquez-Prada, M., Gómez, J. B., & Pacheco, A. F. (2004). A model of characteristic earthquakes and its implications for regional seismicity. *Terra Nova*, *16*(3), 116–120. https://doi.org/10.1111/j.1365-3121.2004.00538.x
Mann, H. B., & Whitney, D. R. (1947). On a test of whether one of two random variables is stochastically larger than the other. *Annals of Mathematical Statistics*, *18*(1), 50–60. https://doi.org/10.1214/aoms/1177730491
Mazzotti, S., Leonard, L. J., Cassidy, J. F., Rogers, G. C., & Halchuk, S. (2011). Seismic hazard in western Canada from GPS strain rates versus earthquake catalog. *Journal of Geophysical Research*, *116*, B12310. https://doi.org/10.1029/2011JB008213
Mezcua, J., Rueda, J., & García-Blanco, R. M. (2011). A new probabilistic seismic hazard study of Spain. *Natural Hazards*, *59*(2), 1087–1108. https://doi.org/10.1007/s11069-011-9819-3
Milner, K. R., Page, M. T., Field, E. H., Parsons, T., Biasi, G. P., & Shaw, B. E. (2013). Appendix T—Defining the inversion rupture set using plausibility filters, USGS Open-File Report 2013–1165, 14 pp.
Morrison, D. R., Jacobson, S. H., Sauppe, J. J., & Sewell, E. C. (2016). Branch-and-bound algorithms: A survey of recent advances in searching, branching, and pruning. *Discrete Optimization*, *19*, 79–102. https://doi.org/10.1016/j.disopt.2016.01.005
Mulargia, F., Stark, P. B., & Geller, R. J. (2017). Why is probabilistic seismic hazard analysis (PSHA) still used? *Physics of the Earth and Planetary Interiors*, *264*, 63–75. https://doi.org/10.1016/j.pepi.2016.12.002
Page, M. (2010). Reply to Schwartz and open discussion. *Seismological Research Letters*, *81*, 331.
Page, M., & Felzer, K. (2015). Southern San Andreas Fault seismicity is consistent with the Gutenberg-Richter magnitude frequency distribution. *Bulletin of the Seismological Society of America*, *105*(4), 2070–2080. https://doi.org/10.1785/0120140340
Page, M. T., Alderson, D., & Doyle, J. (2011). The magnitude distribution of earthquakes near Southern California faults. *Journal of Geophysical Research*, *116*, B12309. https://doi.org/10.1029/2010JB007933.
Page, M. T., Field, E. H., Milner, K. R., & Powers, P. M. (2013). Appendix N—Grand inversion implementation and testing, USGS Open-File Report 2013–1165, 38 pp.
Page, M. T., Field, E. H., Milner, K. R., & Powers, P. M. (2014). The UCERF3 grand inversion: Solving for the long-term rate of ruptures in a fault system. *Bulletin of the Seismological Society of America*, *104*(3), 1181–1204. https://doi.org/10.1785/0120130180
Papadopoulos, G. A., Karastathis, V. K., Ganas, A., Pavlides, S., Fokaefs, A., & Orfanogiannaki, K. (2003). The Lefkada, Ionian Sea (Greece), shock (M_w 6.2) of 14 August 2003: Evidence for the characteristic earthquake from seismicity and ground failures. *Earth, Planets and Space*, *55*(11), 713–718. https://doi.org/10.1186/BF03352478
Parsons, T. (2012). Paleoseismic interevent times interpreted for an unsegmented earthquake rupture forecast. *Geophysical Research Letters*, *39*, L13302. https://doi.org/10.1029/2012GL052275
Parsons, T., Console, R., Falcone, G., Murru, M., & Yamashina, K. (2012). Comparison of characteristic and Gutenberg-Richter models for time-dependent $M \geq 7.9$ earthquake probability in the Nankai-Tokai subduction zone, Japan. *Geophysical Journal International*, *190*, 1673–1688. https://doi.org/10.1111/j.1365-246X.2012.05595.x
Parsons, T., & Geist, E. L. (2009). Is there basis for preferring characteristic earthquakes over Gutenberg-Richter distributions on individual faults in probabilistic earthquake forecasting? *Bulletin of the Seismological Society of America*, *99*(3), 2012–2019. https://doi.org/10.1785/0120080069
Parsons, T., Johnson, K. M., Bird, P., Bormann, J. M., Dawson, T. E., Field, E. H., et al. (2013). Appendix C—Deformation models for UCERF3, USGS Open-File Report, 2013–1165, 66 pp.
Petersen, M. D., Moschetti, M. P., Powers, P. M., Mueller, C. S., Haller, K. M., Frankel, A. D., et al. (2014). Documentation for the 2014 update of the United States national seismic hazard maps: USGS Open-File Report 2014–1091, 243 p., doi:https://doi.org/10.3133/ofr20141091.
Priesemann, V., Munk, H. J. M. H. J., & Wibral, M. (2009). Subsampling effects in neuronal avalanche distributions recorded in vivo. *BMC Neuroscience*, *10*, 40. https://doi.org/10.1186/1471-2202-10-40
Rong, Y., Jackson, D. D., & Kagan, Y. Y. (2003). Seismic gaps and earthquakes. *Journal of Geophysical Research*, *108*(B10), 2471. https://doi.org/10.1029/2002JB002334
Schwartz, D. P. (2010). Do large earthquakes on faults follow a Gutenberg-Richter or characteristic distribution?: A characteristic view. *Seismological Research Letters*, *81*, 331.
Schwartz, D. P., & Coppersmith, K. J. (1984). Fault behavior and characteristic earthquakes: Examples from the Wasatch and San Andreas Fault zones. *Journal of Geophysical Research*, *89*(B7), 5681–5698. https://doi.org/10.1029/JB089iB07p05681
Smirnov, N. V. (1933). Estimate of deviation between empirical distribution functions in two independent samples. *Bulletin Moscow University*, *2*, 3–16.
Stein, S., & Newman, A. (2004). Characteristic and uncharacteristic earthquakes as possible artifacts: Applications to the New Madrid and Wabash seismic zones. *Seismological Research Letters*, *75*(2), 173–187. https://doi.org/10.1785/gssrl.75.2.173
Stirling, M., & Gerstenberger, M. (2018). Applicability of the Gutenberg–Richter relation for major active faults in New Zealand. *Bulletin of the Seismological Society of America*: https://doi.org/10.1785/0120160257, *108*(2), 718–728.
Sykes, L., & Ekström, G. (2012). Earthquakes along Eltanin transform system, SE Pacific Ocean: Fault segments characterized by strong and poor seismic coupling and implications for long-term earthquake prediction. *Geophysical Journal International*, *188*(2), 421–434. https://doi.org/10.1111/j.1365-246X.2011.05284.x

Tullis, T. E. (2012). Preface to the focused issue on earthquake simulators. *Seismological Research Letters*, *83*(6), 957–958. https://doi.org/10.1785/0220120122

Wasserstein, R. L., & Lazar, N. A. (2016). The ASA's statement on *p*-values: Context, process, and purpose. *The American Statistician*, *70*(2), 129–133. https://doi.org/10.1080/00031305.2016.1154108

Weldon, R. J. II, Dawson, T. E., Biasi, G., Madden, C., & Streig, A. R. (2013). Appendix G—Paleoseismic sites recurrence Database, USGS Open-File Report, 2013–1165, 73 p.

Weldon, R. J. II, Schmidt, D. A., Austin, L. J., Weldon, E. M., & Dawson, T. E. (2013). Appendix D—Compilation of creep rate data for California faults and calculation of moment reduction due to creep, USGS Open-File Report, 2013–1165, 42 pp.

Wells, D. L., & Coppersmith, K. J. (1994). New empirical relationships among magnitude, rupture length, rupture width, rupture area, and surface displacement. *Bulletin of the Seismological Society of America*, *84*, 974–1002.

Wesnousky, S. G. (1994). The Gutenberg-Richter or characteristic earthquake distribution, which is it. *Bulletin of the Seismological Society of America*, *84*, 1940–1959.

WGCEP (Working Group on California Earthquake Probabilities) (2003). Earthquake probabilities in the San Francisco Bay region: 2002 to 2031.*Open-File Rep*, U.S. Geol. Survival, 03–214.

Wilcoxon, F. (1945). Individual comparisons by ranking methods. *Biometrics*, *1*(6), 80–83. https://doi.org/10.2307/3001968

Williams, H. P. (2013). *Model Building in Mathematical Programming*, (p. 411). West Sussex, England: John Wiley & Sons.

Wolsey, L. A. (1998). *Integer Programming*, (p. 264). Hoboken, NJ: John Wiley & Sons.